

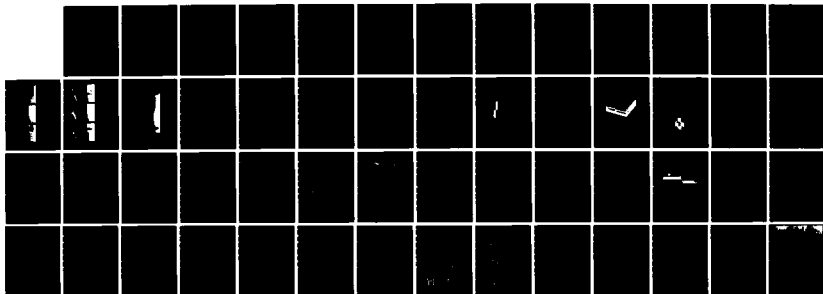
AD-A144 610

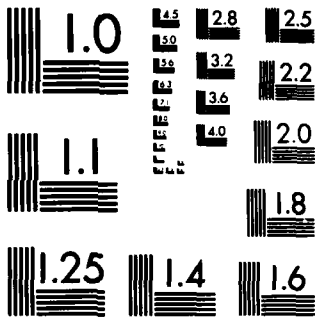
LARGE-SCALE NUMERICAL ANALYSIS OF THREE-DIMENSIONAL  
SEISMIC WAVES(U) WEIDLINGER ASSOCIATES MENLO PARK CA  
G L WOJCIK ET AL. 31 MAY 84 R-8403 AFOSR-TR-84-0691  
F49620-82-C-0002 F/G 8/11

1/1

UNCLASSIFIED

NL





MICROCOPY RESOLUTION TEST CHART  
NATIONAL BUREAU OF STANDARDS-1963-A

AFOSR-TR- 84-08691

WA-CA R 8403

WEIDLINGER ASSOCIATES  
3000 Sand Hill Road  
Building 4, Suite 155  
Menlo Park, California 94025

13

AD-A144 610

**LARGE-SCALE NUMERICAL ANALYSIS  
OF THREE-DIMENSIONAL SEISMIC WAVES**

By  
G. L. Wojcik  
D. K. Vaughan

Prepared for:

Air Force Office of Scientific Research  
Bolling AFB, Washington, D.C. 20332

and

Air Force Geophysics Laboratory  
Terrestrial Sciences Division  
Hanscom AFB, Massachusetts 01731

Approved for  
distribution

DTIC FILE COPY

Final Report  
AFOSR Contract F49620-82-C-0002

For the Period 1 October 1982 to 30 September 1983

84 08 16 027

WA-CA R 8403

**WEIDLINGER ASSOCIATES  
3000 Sand Hill Road  
Building 4, Suite 155  
Menlo Park, California 94025**

**LARGE-SCALE NUMERICAL ANALYSIS  
OF THREE-DIMENSIONAL SEISMIC WAVES**

**By**

**G. L. Wojcik  
D. K. Vaughan**

AIR FORCE OFFICE OF SCIENTIFIC RESEARCH  
NOV 1982  
W. L. ...  
Chief, Technical Information Division

**Prepared for:**

**Air Force Office of Scientific Research  
Bolling AFB, Washington, D.C. 20332**

**and**

**Air Force Geophysics Laboratory  
Terrestrial Sciences Division  
Hanscom AFB, Massachusetts 01731**

**Final Report  
AFOSR Contract F49620-82-C-0002**

**For the Period 1 October 1982 to 30 September 1983**

UNCLASSIFIED

SECURITY CLASSIFICATION OF THIS PAGE (When Data Entered)

REPORT DOCUMENTATION PAGE		READ INSTRUCTIONS BEFORE COMPLETING FORM
1. REPORT NUMBER <b>AFOSR-TR- 84-0601</b>	2. GOVT ACCESSION NO. <b>AD-A144 610</b>	3. RECIPIENT'S CATALOG NUMBER
4. TITLE (and Subtitle) <b>Large-Scale Numerical Analysis of Three-Dimensional Seismic Waves</b>		5. TYPE OF REPORT & PERIOD COVERED <b>Final Report 1 Oct 1982 to 30 Sept 1983</b>
7. AUTHOR(s) <b>G. L. Wojcik D. K. Vaughan</b>		6. PERFORMING ORG. REPORT NUMBER <b>R 8403</b>
9. PERFORMING ORGANIZATION NAME AND ADDRESS <b>Weidlinger Associates 3000 Sand Hill Road, 4-155 Menlo Park, CA 94025</b>		8. CONTRACT OR GRANT NUMBER(s) <b>F49620-82-C-0002</b>
11. CONTROLLING OFFICE NAME AND ADDRESS <b>Air Force Office of Scientific Research Building 410 Bolling AFB, Washington, D. C. 20332</b>		10. PROGRAM ELEMENT, PROJECT, TASK AREA & WORK UNIT NUMBERS <b>61102F 2309/A1</b>
14. MONITORING AGENCY NAME & ADDRESS (if different from Controlling Office) <b>Air Force Geophysics Laboratory/LW Hanscom Air Force Base Bedford, MA 01731</b>		12. REPORT DATE <b>31 May 1984</b>
		13. NUMBER OF PAGES <b>45</b>
		15. SECURITY CLASS. (of this report) <b>UNCLASSIFIED</b>
		15a. DECLASSIFICATION/DOWNGRADING SCHEDULE
16. DISTRIBUTION STATEMENT (of this Report) <b>Approved for public release; distribution unlimited;</b>		
17. DISTRIBUTION STATEMENT (of the abstract entered in Block 20, if different from Report)		
18. SUPPLEMENTARY NOTES		
19. KEY WORDS (Continue on reverse side if necessary and identify by block number) <b>large-scale 3-D finite element analysis      Yucca Flat, Nevada Test Site CRAY-1      full-field synthetic seismograms Basin and Range province      diffractions</b>		
20. ABSTRACT (Continue on reverse side if necessary and identify by block number) <b>→ This report concludes our study of large-scale vectorized numerical analysis applied to time domain seismic wave phenomena in filled basins. Applications include calculations of waves from simple surface or buried sources in a variety of idealized 2-D Basin and Range models (36,000 to 120,000 nodes) described in an interim report, and one large 3-D model (400,000 nodes) from Yucca Flat, Nevada Test Site, described here. Analysis is based on an explicit, finite element, elastic wave solver designed for vectorized execution on the CRAY-1. → cont</b>		

DD FORM 1 JAN 73 1473 EDITION OF 1 NOV 65 IS OBSOLETE

UNCLASSIFIED

SECURITY CLASSIFICATION OF THIS PAGE (When Data Entered)

UNCLASSIFIED

20. ABSTRACT (concluded)

*cont* The primary result of the present 3-D study is that, given the database available from investigations in Yucca Flat, Nevada Test Site, the size of feasible 3-D computational models on the CRAY-1S is adequate to simulate elastic wave fields and interpret arrivals for comparison with existing 3-D ground motion data. The most significant shortcoming is lack of an analytical implementation of the 3-D pressure source.

Synthetic seismograms from a 400,000 element 3-D simulation of the COALORA event at Yucca Flat indicate that a significant source of transverse motion on radial lines through the source is diffraction from a discontinuity in the Rainier Mesa tuff layer across the Yucca fault. This suggests that local geologic inhomogeneities near the source will act as simple diffraction sources--effectively providing secondary seismic sources in the free-field.

Successful time-domain simulations in 3-D are feasible with pipelined supercomputers but optimal processing requires careful tailoring of the algorithm to vectorize inner code loops and eliminate nonessential arithmetic. Theoretical analysis of the simplest cubic finite element shows that the application of eigenvalue-eigenvector concepts, namely, a change of basis, yields a closed form diagonalization of the element mass and stiffness matrices. This provides a significant reduction in the floating point operations count necessary to evolve the element forward in time. In addition, the resulting displacement basis admits a scheme for selective damping of the individual vibrational modes of the element.

UNCLASSIFIED



## CONTENTS

<u>Section</u>		<u>Page</u>
1	INTRODUCTION -----	1
	1.1 Background-----	2
2	GEOPHYSICAL DATA BASE AND MODELS -----	8
	2.1 Yucca Flat Geophysical Models-----	8
	2.2 The 2-D COALORA Model-----	10
	2.3 The 3-D COALORA Model-----	10
3	THE FINITE ELEMENT CALCULATIONS -----	17
	3.1 2-D COALORA Calculation-----	17
	3.2 3-D COALORA Calculation-----	18
	3.2.1 Vertical Velocity Synthetics-----	19
	3.2.2 Head Waves-----	19
	3.2.3 Precursor Waves from Grid Dispersion-----	20
	3.2.4 Radial Velocity Synthetics-----	21
	3.2.5 Transverse Velocity Synthetics-----	21
4	THEORETICAL ANALYSIS OF THE EXPLICIT WAVE SOLVER -----	31
	4.1 The Finite Element Equations--Nodal Basis-----	32
	4.2 The Finite Element Equations--Modal Basis-----	34
	4.3 Viscous Damping-----	37
5	CONCLUSIONS -----	42
	REFERENCES -----	45

## ILLUSTRATIONS

<u>Figure</u>		<u>Page</u>
1.1-1	Velocity functions assumed for basin fills and surrounding bedrock. Basin data compiled by Battis (1981).	4
1.1-2	Vertical velocity seismograms for the piecewise linear velocity models with normal surface traction on the basin centerline.	5
1.1-3	Vertical velocity seismograms for the piecewise linear velocity models with tangential surface traction.	6
1.1-4	Vertical velocity seismograms for the basin-range-basin model with piecewise linear velocity and normal surface traction.	7
2.1-1	Idealized velocity models of the COALORA cross section normal to the Yucca fault.	13
2.1-2	Plan view of the COALORA site showing the Yucca fault, the 6 km east-west line for the 2-D model, and the 2.3 x 2.3 km square for the 3-D model.	14
2.3-1	Yucca Flat 3-D model showing Yucca fault and COALORA shot location. Model is 4.6 km on a side and 1.2 km deep, with 125 x 125 x 25 = 390,625 elements.	15
2.3-2	Illustrations of output lines over source cavity in Yucca Flat model, and the seven element 3-D source cavity.	16
3.1-1	The 2-D COALORA model and vertical velocity seismograms calculated on the free surface. The source cavity is pressurized at $t = 0$ . The static water level is indicated by SWL.	24
3.1-2	Horizontal (radial) velocity seismograms over the 2-D COALORA model. Magnifications are indicated above the individual traces.	25
3.1-3	Vertical velocity seismograms for a 10 Hz wavelet at 600 m and 2619 m ranges east and west of Yucca fault showing calculated time delays.	26
3.2-1	Vertical velocity synthetic seismograms with magnifications indicated on right. Peak velocity is $.367 \times 10^{-7}$ m/s and the upper set is for diagonal lines while the lower is for global lines.	27

ILLUSTRATIONS (Concluded)

<u>Figure</u>		<u>Page</u>
3.2-2	Radial (horizontal) velocity synthetics. Peak velocity is $.23 \times 10^{-7}$ m/s.	28
3.2-3	Transverse velocity synthetics. Peak velocity on global lines is $.068 \times 10^{-7}$ m/s and on the diagonals it is $.0107 \times 10^{-7}$ NW-SE and $.026 \times 10^{-7}$ SW-NE.	29
3.2-4	Drawing of the source and fault discontinuity in the tuff layer showing origin of primary and secondary diffracted waves from the fault edges.	30
4.1-1	The Cartesian grid and element coordinate system assumed for isotropic media.	39
4.2-1	The eight mass matrix deformation modes of a cube, for the $\zeta_1$ direction. Extension and shear are modes of the first kind, while bending deformations are modes of the second kind.	40
4.2-2	The decomposition of extension and shear modes into Poisson stretch, pure shear and rotation modes, shown here for the $\zeta_1$ direction.	41

## 1.0 INTRODUCTION

This final report concludes our study of large-scale vectorized numerical analysis applied to time domain seismic wave phenomena in filled basins. Applications include calculations of waves from simple surface or buried sources in a variety of idealized 2-D Basin and Range models (36,000 to 120,000 nodes) and one large 3-D model (400,000 nodes) from Yucca Flat, Nevada Test Site. Analysis is based on an explicit, finite element, elastic wave solver designed for fully vectorized execution (vector processing of code loops) on the CRAY-1. This combination of an explicit solver and the new generation of supercomputers permits full wave solutions in inhomogeneous models 10 to 100 times faster and larger than feasible using conventional solvers on scalar mainframe computers (e.g., CDC 7600).

The study is motivated by interest within the U.S. Air Force in calculations of high frequency wave fields in realistic models of basins and basin-like geology. Well controlled models generally include smooth wave speed variations within each material, as well as discontinuities, curved interfaces, pinch-outs, faults, sharp corners, irregular topography and surface layers. Typical analytical methods require significant approximations to make these problems tractable. For example, simplifying assumptions on the wave field often involve high-frequency asymptotics and ray tracing which usually neglect diffractions and surface waves, or sometimes the replacement of elastic by acoustic media in discrete numerical models. Physical idealizations can lead to plane, layered models which admit semi-analytic halfspace solutions; or piecewise constant material properties and smooth interfaces amenable to boundary integral methods; or discrete approximations but with reduced model size to fit into fast computer memory. However, with the computational power afforded by explicit methods and supercomputers, these idealizations are often unnecessary and more complete or accurate solutions are available. In any case, large-scale calculations are useful in general modeling applications and numerical experiments, as well as the evaluation of modeling idealizations.

Research goals of the study are two-fold. First is to perform large-scale calculations and seismic interpretation for a number of interesting geologic models. Second, in support of the calculations, is to study

theoretically the numerical/computational basis for discrete hyperbolic wave solvers (explicit finite difference/finite element methods) and to increase their utility in seismic applications, and their compatibility with super-computer architecture. This latter goal includes an evaluation of present capabilities on available CRAY hardware.

A previous report addresses these goals in the context of 2-D modeling of some typical Basin and Range geology. An overview of results is presented in 1.1 below. The present report is concerned principally with 3-D calculations for a model of the recent COALORA test in Yucca Flat, Nevada Test Site. Due to the complexities associated with 3-D modeling and interpretation, the Yucca Flat site, suggested by Stump (1983), was chosen over other candidate sites because an excellent geophysical data base exists, incorporating seismic, gravity and well log data. The geophysical data base and models are discussed in Section 2 and the 2-D and 3-D finite element calculations are described in Section 3. A theoretical analysis of the explicit wave solver algorithm is contained in Section 4. A brief discussion and conclusions complete the report in Section 5.

#### 1.1 BACKGROUND

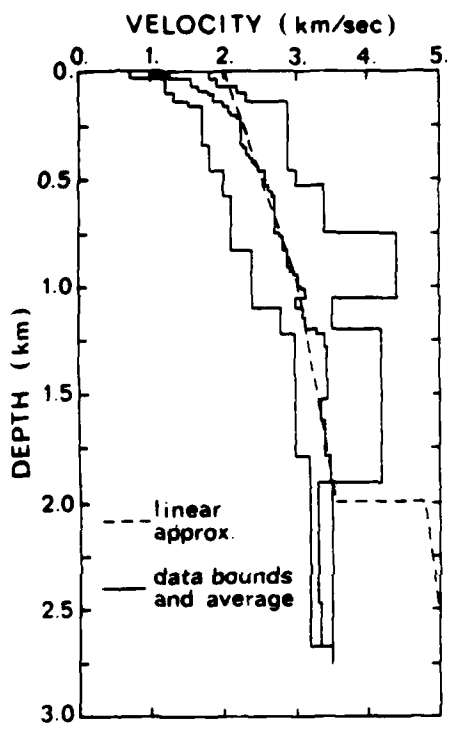
The following is a summary of results from an interim report, Wojcik, et al. (1982), containing a numerical analysis of 2-D basins typical of the Basin and Range province. Calculations were performed to study the effects of basin edge geometry on the reflection, transmission and diffraction of body and surface waves excited by surface sources. Normal and tangential surface tractions were applied on the model centerlines and synthetic seismograms generated by convolving a 2 Hz wavelet with numerical Green's functions recorded at closely spaced stations over the surface. Seismic velocity functions used piecewise linear and piecewise constant approximations to a suite of functions compiled by Battis (1981) from available Basin and Range geophysical data, Fig. 1.1-1.

Symmetric basin models with three types of flank structure were examined first. The models and synthetic seismograms for normal and tangential surface loading are illustrated in Fig. 1.1-2 and 1.1-3, respectively. These and other calculations showed a number of quantitative differences between a steep faulted flank, an echelon faulted flank and a dipping flank. Basin

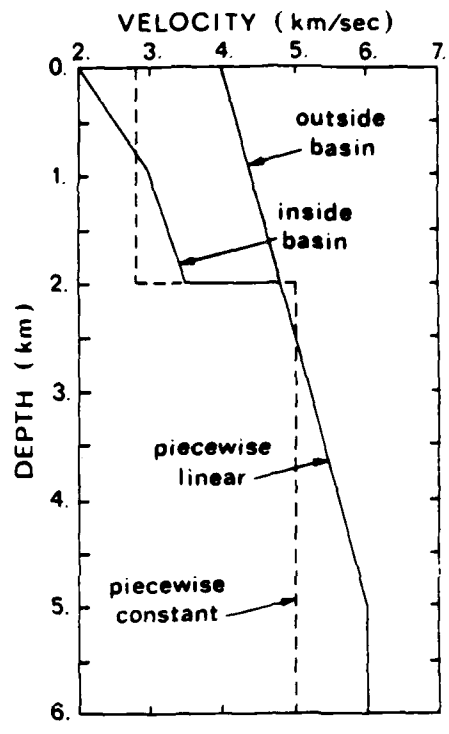
edges are efficient transmitters of Rayleigh waves, apparently independent of edge details; however, geometry has a strong effect on Rayleigh wave reflection. Shear waves outside the basin depend markedly on source type and edge geometry due to mode conversions there. The strong shear phase generated by the tangential source is converted primarily to S-waves at the edge, whereas the shear phase from the normal source converts most of its energy to Rayleigh waves.

A model of two basins separated by a mountain was also examined. This basin-range-basin model, Fig. 1.1-4, extended the above results for a single basin and provided insight into the type and strength of signals communicated between basins. The finite element idealization had 120,000 elements, required 20 minutes of central processor time (overnight cost, \$100.) to propagate the Rayleigh wave across it, and demonstrated that large-scale full wave field calculations are practical on the CRAY-1.

The major result of the finite element theoretical work was that, in the context of Cartesian (rectangular) finite element/finite difference grids, the governing equations on the element level can be greatly simplified by linear transformation and formulated so as to admit selective seismic damping on pure shear and dilatational modes of deformation. The transformation is to a set of generalized coordinates based on the allowed element vibrational modes. The application of linear transformations on the global as well as local level offers the possibility of further reducing arithmetic operation counts, thereby increasing execution speed of the algorithm.

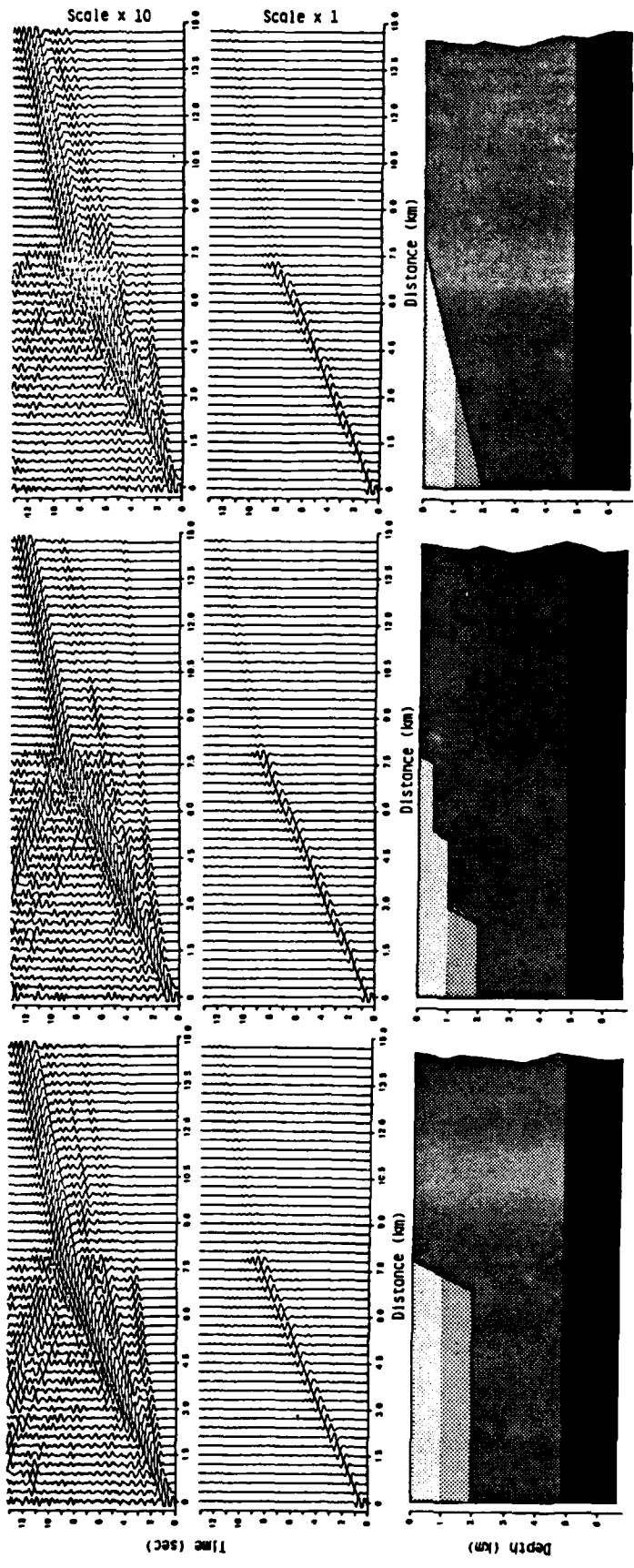


a. BASIN VELOCITY MODEL



b. UPPER CRUST VELOCITY MODEL

Figure 1.1-1 Velocity functions assumed for basin fills and surrounding bedrock. Basin data compiled by Battis (1981).

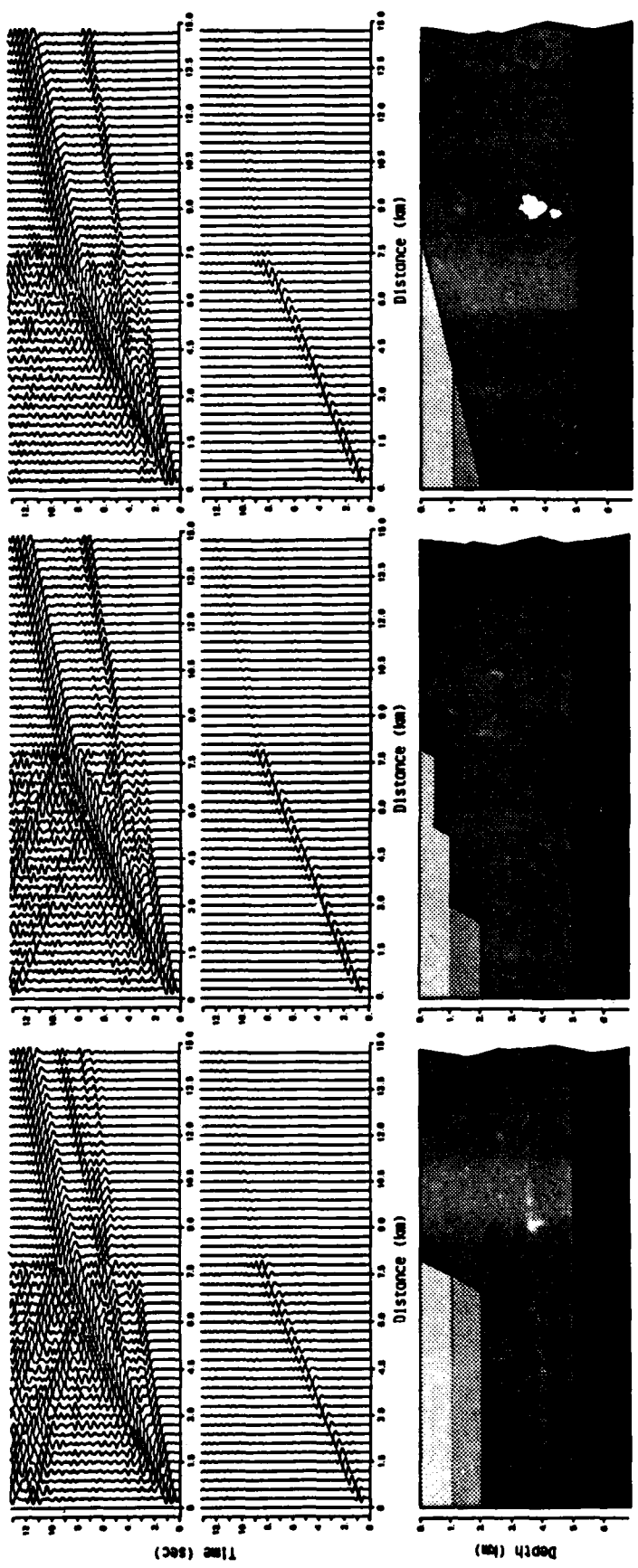


a. Steep faulted flank

b. Echelon faulted flank

c. Dipping flank

Figure 1.1-2 Vertical velocity seismograms for the piecewise linear velocity models with normal surface traction on the basin centerline (left side of figures).



a. Steep faulted flank      b. Echelon faulted flank      c. Dipping flank

Figure 1.1-3 Vertical velocity seismograms for the piecewise linear velocity models with tangential surface traction.

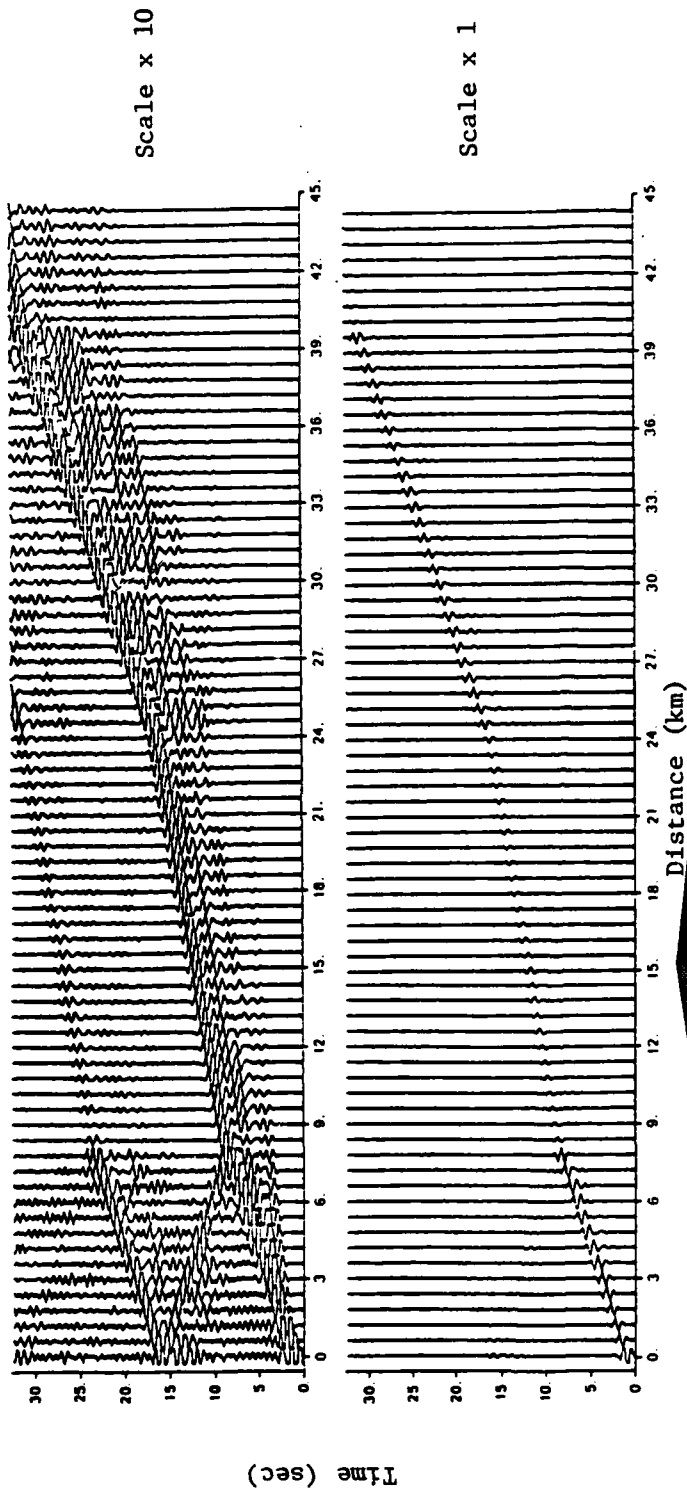


Figure 1.1-4 Vertical velocity seismograms for the basin-range-basin model with piecewise linear velocity and normal surface traction.

## 2.0 GEOPHYSICAL DATA BASE AND MODELS

Full wave field seismic calculations are much more complicated in 3-D than in 2-D. The reasons are that 3-D geologic data and 2-D surface modeling and input processing are necessary, finite element data storage and element processing time both increase substantially, and the amount and complexity of output processing grows manyfold. Despite these added complexities, with well designed pre- and post-processors and a general 3-D finite element solver, 3-D problems can be reasonably modeled, solved and interpreted. There remains the question of size and utility for the scale of Air Force applications.

An answer to this question of utility--whether large-scale 3-D simulations are practical on today's supercomputers--requires first and foremost a good geophysical data base. In other words, a well controlled, practical geologic model, preferable with seismic data available for comparison with synthetics. Yucca Flat, Nevada was chosen on the basis of data collected from AFOSR-sponsored research concerning near-field observations of significant azimuthal variations in recorded ground motion, Stump and Reinke (1983), and far-field observations of systematic deviations in peak body wave magnitude estimates (mb), Ferguson and Herrin (1982). Other good sources of data are the detailed geophysical investigations done in Yucca Flat to insure shot containment, Cogbill and App (1983).

With the geologic model controlled from the above studies, it is next a matter of gridding the model, i.e., coding the 3-D finite element discretization, and running it on a CRAY. This is accomplished in our work using a general purpose, explicit finite element code called FLEX, consisting of standard FORTRAN subroutines designed for optimized execution on scalar as well as vector machines. For the 2-D problems described above, a standard CRAY-1 (one million words of memory) was sufficient. However, for 3-D much more memory is required and at least a CRAY-1S (three million words) is necessary.

### 2.1 YUCCA FLAT GEOPHYSICAL MODELS

Our desire to perform calculations in a well controlled model led to selecting the north-central part of Yucca Flat, in the immediate neighborhood of a recent underground nuclear explosion, COALORA. Extensive near-field ground motion data have been collected from this shot in a cooperative effort

(Air Force Weapons Lab, Los Alamos National Lab and University of California, Berkeley) to extend the observational data base from contained nuclear explosions, Stump and Reinke (1983). To constrain their COALORA propagation model, Stump and Reinke used a coarser 3-D basin model developed by Ferguson and Herrin (1982) from a variety of geophysical data. This was refined in the neighborhood of COALORA using geological cross sections and acoustic logs provided by Allen Cogbill and Fred App of the Containment Group at LANL.

The resulting propagation model developed by Stump and Reinke, Fig. 2.1-1, is assumed to be uniformly layered east and west of the fault. Major features of the model include the Yucca fault dipping approximately 72 degrees to the east in a 350-500 meter layer of alluvium overlying 600 meters of interbedded tuffs--all overlying Paleozoic rock at depths near 1 km. Data from two boreholes indicate that the interbedded tuffs have vitrified layers with impedance jumps of a factor of two or more. These are modeled by a single cap layer of Rainier Mesa tuff in Fig. 2.1-1. The water table is placed at a depth of 600 meters.

Actually, the Rainier Mesa formation dips 15-18 degrees to the west and is shallower to the north. Also, the alluvium-tuff interface is highly irregular over much of the basin, due in part to tectonic movement, Fernald et al. (1967). In the COALORA model, smooth depth changes and 3-D variations were ignored with respect to the abrupt change at the Yucca fault, allowing the authors to calculate full-wave synthetic seismograms in the uniformly layered eastern and western halfspace idealizations.

Location of the shot with respect to the Yucca fault is drawn in Fig. 2.1-2 and indicates a smooth, right-lateral offset in the fault trace (identified in the field by a low scarp over most of its 25 km length) within .5 km southeast of the shot epicenter. This is a significant 3-D feature, being so close to the shot, and provides the central structural element of our 3-D geologic model. The secondary element is the major discontinuity between tuff and Paleozoic rock. A coarse model of the contact surface was provided by Ferguson (1983), based on studies of gravity, borehole and seismic reflection data. Limited resolution of the data smooths out any local details, including the Yucca fault which is known to have a vertical offset of 100-200 meters at the Paleozoic contact.

## 2.2 THE 2-D COALORA MODEL

Before examining the 3-D model in Yucca Flat, a 2-D plane strain model of the COALORA site was investigated to compare results with layered halfspace calculations in Stump and Reinke (1983), as well as recorded seismograms. The shot was located in alluvium at a depth of 280 meters, just above the Rainier Mesa tuff layer on the western side of Yucca fault. Lateral scale of the model covers the range of most fielded seismic instruments--three kilometers east and west of the shot. Model depth is 1.5 km, 400-500 meters into the underlying Paleozoic rock. To mimic an infinite halfspace, normal impedance boundary conditions are applied to the two sides and bottom of the finite element grid. This yields a simple but effective absorbing boundary which is easily vectorized--in contrast to some other boundary formulations attempted.

The number of elements in the model is chosen to achieve a given frequency resolution for the slowest body or surface wave. Assuming negligible excitation of Rayleigh waves due to source depth, the slowest wave is the shear body wave in the alluvium, where  $V_s = .98$  km/s. Assuming 10 Hz as the highest frequency of interest in this calculation yields a minimum shear wavelength of about 98 meters. A rule of thumb for explicit finite element algorithms is that at least ten elements are necessary per wavelength to support a wave with minor dispersion. Therefore, an element dimension of 9 meters was used, giving 167 by 666 square elements in a 1.5 by 6 km model, a total of 111,222 elements.

The line source is a pressurized two-dimensional cavity of elements through the COALORA shot point, 280 meters below the surface in alluvium and 300 meters west of Yucca fault. Output in the form of synthetic seismograms is obtained by convolving the calculated velocity response on the free surface (from the unit pressure step) with a 10 Hz wavelet. No instrument response is included. The 10 Hz velocity wavelet is a higher frequency signal than would be expected from shots in alluvium, Haskell (1967), but facilitates the visual separation of arrivals in the synthetics.

## 2.3 THE 3-D COALORA MODEL

The three-dimensional geologic model in Yucca flat is contained within a 3-D rectangular box, 1.2 km deep and 4.6 km on a side, centered on the COALORA

shot point. Principal features of the model are the Yucca fault with about 800 meters of right offset in the fault trace south of the shot, and the Paleozoic contact surface showing significant depth variation within a 3 km radius. The fault trace is approximated by a straight north-south line with a linearly offset segment, i.e., a piecewise linear trace, and the resulting fault surfaces dip 72 degrees to the east. The Paleozoic contact is assumed merely to truncate the alluvium and tuff basin fill from below; there is no attempt to model conformable layers over the contact surface. A drawing of the resulting 3-D model is shown in Fig. 2.3-1.

When going from 2-D to 3-D modeling, if it is necessary to maintain the same frequency resolution, the number of elements goes up tremendously. For example, to extend the 6 x 1.5 km 2-D COALORA model ( $666 \times 167 = 111,222$  elements) to a 6 x 6 x 1.5 km 3-D model with the same frequency resolution would require  $666 \times 111,222 = 74$  million elements. This is over two orders of magnitude larger than the size currently feasible with in-core processing on the largest CRAY supercomputer, the CRAY-1S, with 3 million words of memory. The data structure of FLEX, the finite element code used for these calculations, permits the processing of 500,000 3-D elastic, small-displacement elements in 3 megawords of memory. System overhead and other uncontrollable factors reduce this number to slightly less than 400,000 elements. Assuming an overall model aspect ratio (length or width to depth) of 5, the 400,000 available elements yield a block  $125 \times 125 \times 25 = 390,625$ .

Clearly, the time and length scales of our 3-D model must be increased substantially over those of the 2-D model to fit into the CRAY-1S. Lowering the maximum shear wave frequency resolution from 10 Hz to 2.5 Hz increases the element size by the same factor, and decreases the number of elements by  $4^{**3}=64$ . This necessitates only a moderate reduction of the 2-D model dimensions. The final model is 1.2 x 4.6 x 4.6 km--discretized into  $125 \times 125 \times 25 = 390,625$  cubic elements, 37 meters on a side with a maximum frequency resolution of 2.6 Hz for shear waves in the alluvium.

The elastic point source is represented by a 3-D cavity of elements enclosing the shot point. The cavity is pressurized by a unit step at  $t=0$  and three-component velocities are recorded at points on four lines over the free surface. The cavity consists of three elements crossing on three orthogonal lines. This provides an approximation intermediate between the circularized

source of the 2-D calculation and the three dipole forces equivalent to an explosive point source, e.g., Love (1944). Lines are oriented north-south, east-west and along the two diagonals, northwest-southeast and northeast-southwest. The source cavity and output lines are illustrated in Fig. 2.3-2.

Synthetic seismograms are calculated by convolving the recorded velocities with a 3.5 Hz wavelet, which is closer to the expected frequency content of the COALORA shot than the 10 Hz wavelet applied in the 2-D calculation. This frequency is 1 Hz higher than the allowable shear wave frequency in the alluvium but, because P-waves are the principal phases there and are well modeled, the higher frequency is used to enhance the temporal separation of these phases in the synthetics.

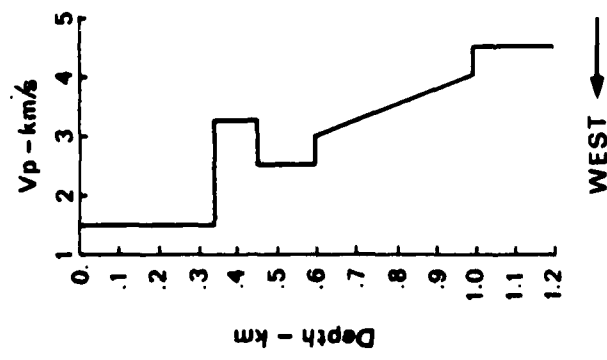
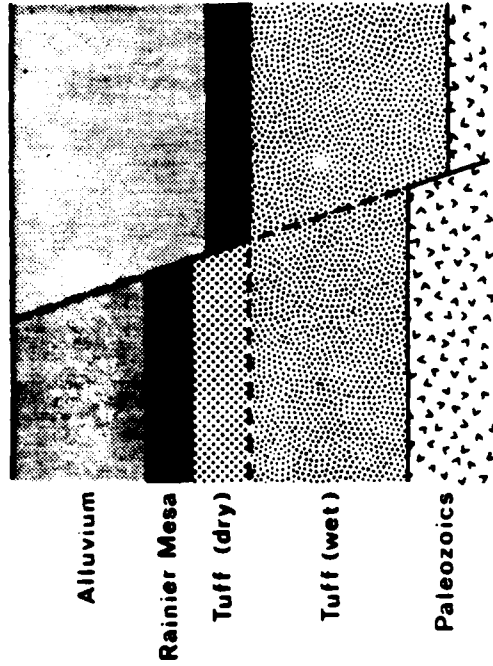
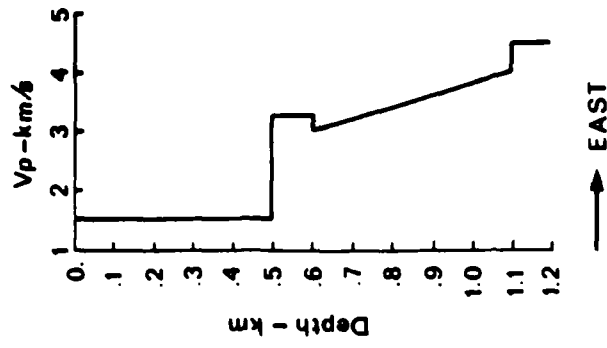


Figure 2.1-1 Idealized velocity models of the COALORA cross section normal to the Yucca Fault (from Stump and Reinke (1983)).

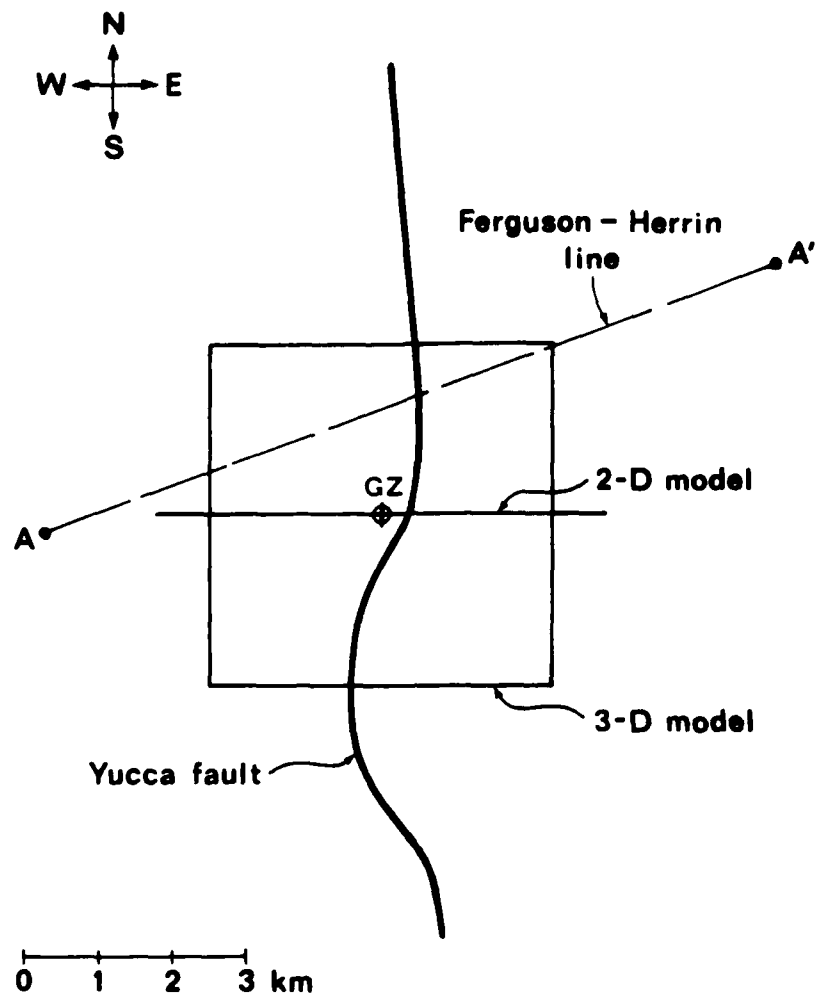


Figure 2.1-2. Plan view of the COALORA site showing the Yucca fault, the 6 km east-west line for the 2-D model, and the 2.3 x 2.3 km square for the 3-D model. For reference, the line examined in detail by Ferguson and Herrin (1982) is also included.

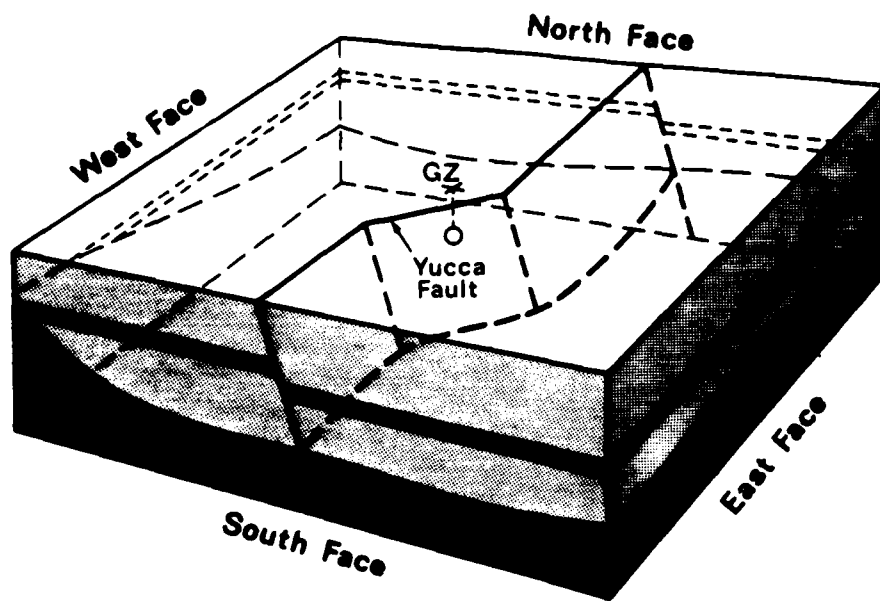
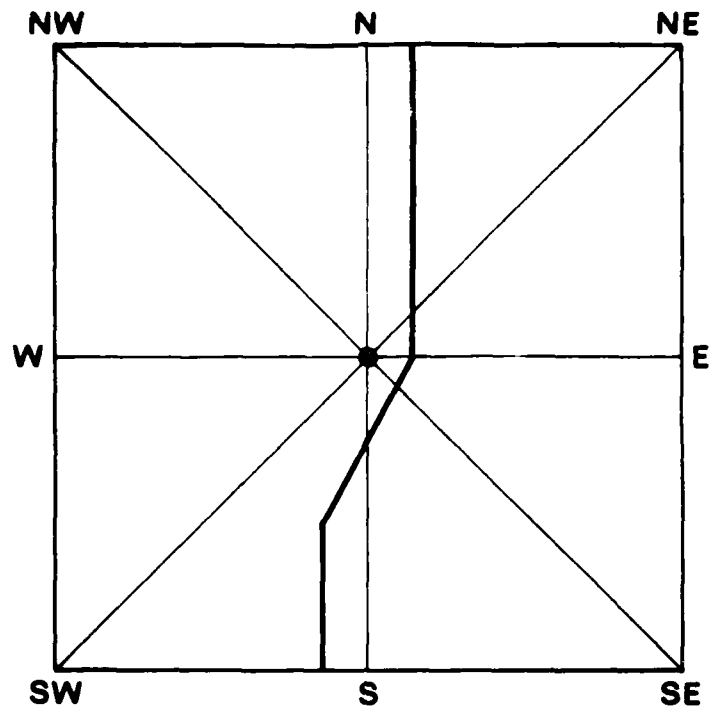
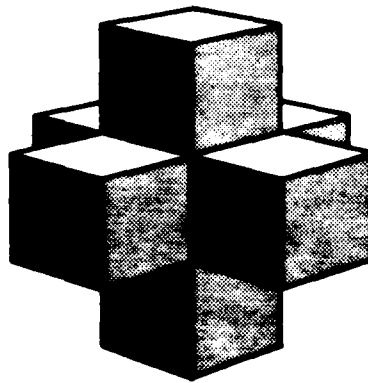


Figure 2.3-1. Yucca Flat 3-D model showing Yucca Fault and COALORA shot location. Model is 4.6 km on a side and 1.2 km deep, with  $125 \times 125 \times 25 = 390,625$  elements.



Output lines over free surface



Source Cavity

Figure 2.3-2. Illustrations of output lines over source cavity in Yucca Flat model, and the seven element 3-D source cavity.

### 3.0 THE FINITE ELEMENT CALCULATIONS

The calculations described here were performed on a CRAY-1S at the Los Alamos National Laboratory. Computer time was generously provided by the Containment Group at the Lab. Because the CRAY-1S is on a restricted partition, it was not accessible from our remote site. Allen Cogbill of the Containment Group provided the essential interface by submitting run files and making output files accessible. Raw output data were transmitted over the phone between Los Alamos and Menlo Park and all post-processing was done on an inhouse mini-computer.

#### 3.1 2-D COALORA CALCULATION

The 2-D model and synthetic velocity seismograms are shown in Figs. 3.1-1 and 3.1-2 for vertical and radial components, respectively. The seismograms (particle velocity versus time) are plotted vertically over each receiver point on the model surface. Amplitude in each record is scaled to the maximum first arrival over the model. Scale magnification factors are indicated above the seismograms. The wavelet has a duration of about .18 seconds and a wavelength of approximately 270 meters in the alluvium. The receiver point near ground zero is offset to the east slightly, explaining the radial motion just above the shot in Fig. 3.1-2.

Within a range of 1 km, the first arrival is seen to be the direct wave through the alluvium. Beyond 1 km, a much weaker wave, apparently a head wave from the faster vitrified tuff layer (Rainier Mesa formation), precedes the direct wave. Just above the shot, the vertical record (Fig. 3.1-1) shows a phase shifted wavelet--from an initial zero phase input--caused by interference between the direct wave and that reflected from and reverberating in the tuff layer immediately below the source. No significant reflection from the 1 km Paleozoic interface is evident in the records near the calculated .69 second arrival time. Radial records indicate a strong reflection within a range of 300 meters, arriving at .45 to .5 seconds and comparable in amplitude to the direct wave. This appears to be a reflection from the water table at a depth of 500 meters. Comparing vertical and radial records overall, radial motion is stronger and more coherent than vertical motion, and records to the west are somewhat more complicated than those to the east.

Referring now to the radial synthetics, Fig. 3.1-2, the Yucca fault does not appear to exert a strong local influence on the model response. No direct

diffractions, attributable to the fault discontinuity in the Rainier Mesa tuff layer are evident in the records. Although certainly present, they are obscured by the direct and reflected arrivals. Differences between east and west records are probably due to the respective depths of alluvium rather than to diffractions and scattering from the fault itself. Principal differences are: direct waves in alluvium decay faster to the west (see the unmagnified set of radial synthetics), and also to the west there appears a phase between 1 and 1.8 km range, arriving from 1.3 to 1.7 seconds which is absent to the east.

Regarding phase velocities, measurement from the records gives the direct wave in alluvium at 1.53 km/s, but the head waves arriving beyond 1 km yield 3.75 km/s. The alluvium phase velocity is 2 percent greater than the wave speed and within modeling error bounds. However, the head wave velocities are clearly too high to be associated with the 3.25 km/s Rainier Mesa tuff, and are instead due to refractions from the saturated tuff below the water table. True head waves from the Rainier Mesa tuff are just noticeable as first arrivals between 1 to 1.6 km.

Some limited timing comparisons east and west of the fault can be made from the records to later compare with results from Stump and Reinke (1983). At a range of 567 meters, travel time is 435 ms and there is no difference between east and west--as would be expected at this close range with no intervening homogeneities in the alluvium. At a range of 2.62 km, the timing discrepancy is 56 ms, retarded to the east and due to the depth difference. The records are shown in Fig. 3.1-3.

### 3.2 3-D COALORA CALCULATION

Results of the 3-D calculations are presented in synthetic velocity seismograms, Figs. 3.2-1 through 3.2-3, for vertical, radial and transverse components. The synthetics consist of 42 individual seismograms equally spaced on lines passing over the shot. The west-east and south-north (global) lines are 4.5 km long (111 meter spacing), and the diagonal lines are 6.36 km (157 meter spacing), oriented southwest-northeast and northwest-southeast. Three sets of synthetics are displayed for each line, with magnifications of 1, 20 and 2000. The high magnification is used to examine the weak refracted phases. Duration of the synthetics is 1.98 seconds after pressurization of the cavity.

### 3.2.1 Vertical Velocity Synthetics

Vertical velocity synthetics are shown in Fig. 3.2-1 for the four lines. Because the predominant input frequency is a third of that used in the 2-D synthetics, wavelets are three times longer, hence less distinct and interfere to a greater degree. The strongest motion is found over the shot point at around .4 seconds, caused by constructive interference of the direct wave and reflected wave from the layer of Rainier Mesa tuff. Referring to the unmagnified synthetics, ground motion decays rapidly with range--due in part to scaling by peak interference amplitude rather than peak direct wave amplitude.

At a magnification of 20 the synthetics clearly show the direct wave as first arrival out to .9 km, at a measured phase velocity of 1.52-1.58 km/s on all lines. Beyond a range of 1.35 km the first arrival is a refraction and the phase velocity apparently depends on the depth of alluvium under the line observed. On the S-N line, phase velocity,  $V$  is 3.1 km/s to the south and 3.26 km/s to the north. On the W-E line,  $V$  is 3.1 km/s to the east and 3.26 km/s to the west. From Fig. 2.3-1, the south and east ends lie on .5 km of alluvium on the downthrown side of the fault, and the north and west ends are over .35 km of alluvium on the upthrown side. Therefore, calculated phase velocities are lower on the down side (east and south) and higher on the up side (west and north). By overlaying the synthetics so that east is plotted over south and west over north, we find that all arrivals are coincident, independent of range.

On the diagonal lines, also in Fig. 3.2-1, the refracted phases are less distinct. Approximate measurements of slope on the synthetics at a magnification of 20 give phase velocities of the first discernable arrivals as 3.25-3.32 km/s on the northwest and southwest ends, respectively. Consequently, phase velocities on the diagonals do not show the trend nor the disparity noted above between up and down sides of the fault. On the southwest end of the SE-NE line the phase velocity is seen to increase significantly between -2.5 and -3.2 km. This is attributed to a refracted wave in the shallow Paleozoic rock underlying the southwest corner of the model, Fig. 2.3-1.

### 3.2.2 Head Waves

To see the earliest arriving signals in the finite element model, we must examine the synthetics under very high magnification. At 2000X there is

a clear first arrival which precedes all of the much stronger arrivals described above. Referring to the south-north line in Fig. 3.2-1, phase velocities are found to be 3.0 km/s on the south end (down side) and 2.7 km/s on the north end (up side)--in contrast to the trend observed above for later but stronger arrivals. Physically, these first arrivals should be head waves from the Rainier Mesa tuff layer.

Calculating the theoretical head wave arrival time at a range of 1.8 km gives .76 seconds at the north end and .85 seconds at the south end. Measured times from the seismograms at this range are .74 seconds and .83 seconds north and south, respectively, within 2-3 percent of the theoretical. Therefore, in terms of arrival times the phase is a refraction in the tuff layer, but phase velocities are 8 percent and 16 percent below the theoretical value of 3.25 km/s. Discrepancies in  $V$  are caused in part by the 3-D finite element discretization, which only uses three elements through the thickness to represent the high speed tuff layer. This is clearly adequate to model arrival times within a few percent, but measured phase velocities, which depend on the angle of incidence of the wave from below, are more sensitive to the coarse discretization in the layer.

### 3.2.3 Precursor Waves from Grid Dispersion

Further examination of the 2000X synthetics shows that just above the shot, the earliest arrival time is .045 seconds, compared to the theoretical body wave time of .15 seconds. This discrepancy is associated with the finite element discretization in general, and the 3-D source region in particular.

When the source cavity is pressurized, in addition to the radial modes of an ideal spherical cavity, extraneous deformational modes are generated. Most of these propagate at the appropriate body wave speed and decay rapidly with range--however, weak precursors caused by grid dispersion will always propagate one element per timestep. For a timestep of .0066 seconds, with seven elements between the free surface and the shallowest pressurized element, the theoretical arrival time is .046 seconds (versus .045 seconds measured from the seismograms) for an apparent body wave speed of 5.64 km/s.

The precursors may therefore be identified in the 2000X seismograms as the first phase observed immediately above the source. Included in these precursors is the so-called hourglass mode which is suppressed using a special hourglass stiffness parameter in the finite element algorithm. This

spurious mode is only significant (under high magnification) in the immediate neighborhood of the source. It will always be present to some degree and is most prevalent when only a few elements are contained in the source cavity, one pressurized element being the worst case. Hourglassing will be discussed further in the theoretical development.

#### 3.2.4 Radial Velocity Synthetics

Radial velocity components on the global west-east and south-north lines are shown in Fig. 3.2-2. The unmagnified synthetics on global lines indicate that radial motion is more coherent and decays less rapidly with range than vertical motion on the same line. Comparing the magnified radial records to the verticals discussed in 3.2-1 shows essentially the same first arrival times and phase velocities over each end of the lines. Within .9 km of the shot, radials on the diagonal lines exhibit a stronger, slightly earlier direct arrival. The implication is that vertical and radial motions are well correlated, i.e., surface ground motions arise from the same incident body wave phases.

#### 3.2.5 Transverse Velocity Synthetics

Transverse synthetics on the global lines in Fig. 3.2-3 show relatively weak arrivals with peak motions 25-30 percent of the radial component. The transverse arrivals appear to correlate with vertical and radial components of motion. Careful comparison shows that transverse peaks are retarded by .15 seconds on both ends of the W-E line, while on the S-N line peaks are coincident on the south end and retarded by .15 seconds on the north end. Motion asymmetry on the S-N line is clearly visible in the 20X synthetics, with earlier, stronger transverse velocities on the south end. The asymmetry might be attributed to wave interaction at the fault crossing, south of the shot--probably diffractions from the obliquely oriented discontinuity in the Rainier Mesa tuff layer. No such discontinuity is crossed on the north end and the transverse arrivals are much weaker there. On the W-E line the arrivals are weak on both ends, although the east line crosses the fault perpendicular to the tuff discontinuity and the west line does not cross at all. Therefore, waves incident on the fault trace at an oblique angle appear to

excite stronger transverse motions by diffraction from the edge of tuff layer discontinuities across the fault.

Referring now to transverse arrivals on the diagonal lines, also in Fig. 3.2-3, there is a marked difference in arrival times between synthetics on the diagonals and those on the global lines. At 1X the transverse velocity is clearly higher on the southeast and northeast ends of the lines. These ends both cross the fault trace obliquely and appear to support the hypothesis that diffractions from oblique crossings of the discontinuity are responsible for the stronger transverse arrivals.

The transverse phases on the diagonals also show a large time delay in comparison to phases on the globals. If diffraction is the principal source of these phases, then the retarded arrivals should agree with theoretical timing from the source cavity to the fault edge and up to the surface. The first arrival at the fault is a weak head wave through the Rainier Mesa tuff layer at .12 seconds, and travel time of the resulting diffracted wave to the free surface above the shot is .37 seconds--giving a total time delay of .49 seconds. Measured delay in the 20X synthetics is .45 seconds for the weak precursors and about .5 seconds for the true arrival. This strongly suggests that diffractions from the fault are the principal source of transverse phases on the diagonal lines, which is further supported by the skewed appearance of the synthetics, i.e., the apparent source is shifted to the right, consistent with the direction and approximate range of the diffracting fault edge from the source cavity.

The strong asymmetry in arrival times on either end of the diagonal lines also appears to be caused by the fault. Measured phase velocities on the east (down) side of the fault (right side of the synthetics) are 1.55-1.7 km/s on both lines, while on the west (up) side they are 3.3-3.5 km/s. Therefore arrivals to the east propagate through the slow alluvium, and to the west they propagate through the faster tuffs. The reason that no wave energy is seen in the tuffs to the east is that only weak secondary diffractions (diffractions of diffractions) from the up side of the fault edge can couple into the down-thrown layers. In contrast, diffracted energy from the discontinuity is coupled directly into the layer on the west side. This is illustrated in Fig. 3.2-4.

Comparing transverse motion on the diagonals to that on the globals shows earlier and stronger arrivals on the global W-E and S-N lines. The discrepancy

is caused in part by a one-half element offset of the global lines from the true shot center, causing an erroneous transverse component which is strongest near the source. The diagonal lines pass directly over the shot center. Quantitatively, the diagonal line transverse motions are 20-30 percent of the global line motions and the half element offset does not seem to account for the full discrepancy.

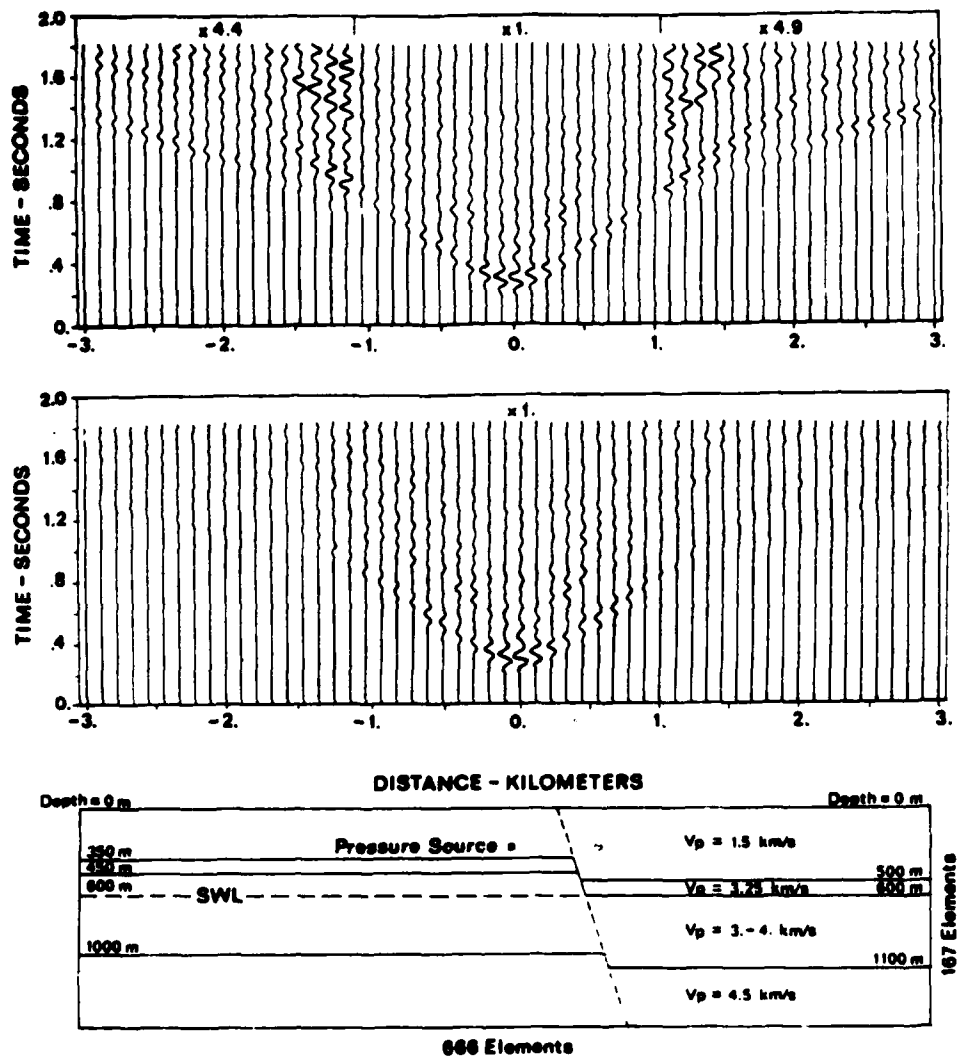


Figure 3.1-1. The 2-D COALORA model and vertical velocity seismograms calculated on the free surface. The source cavity is pressurized at  $t = 0$ . The static water level is indicated by SWL.

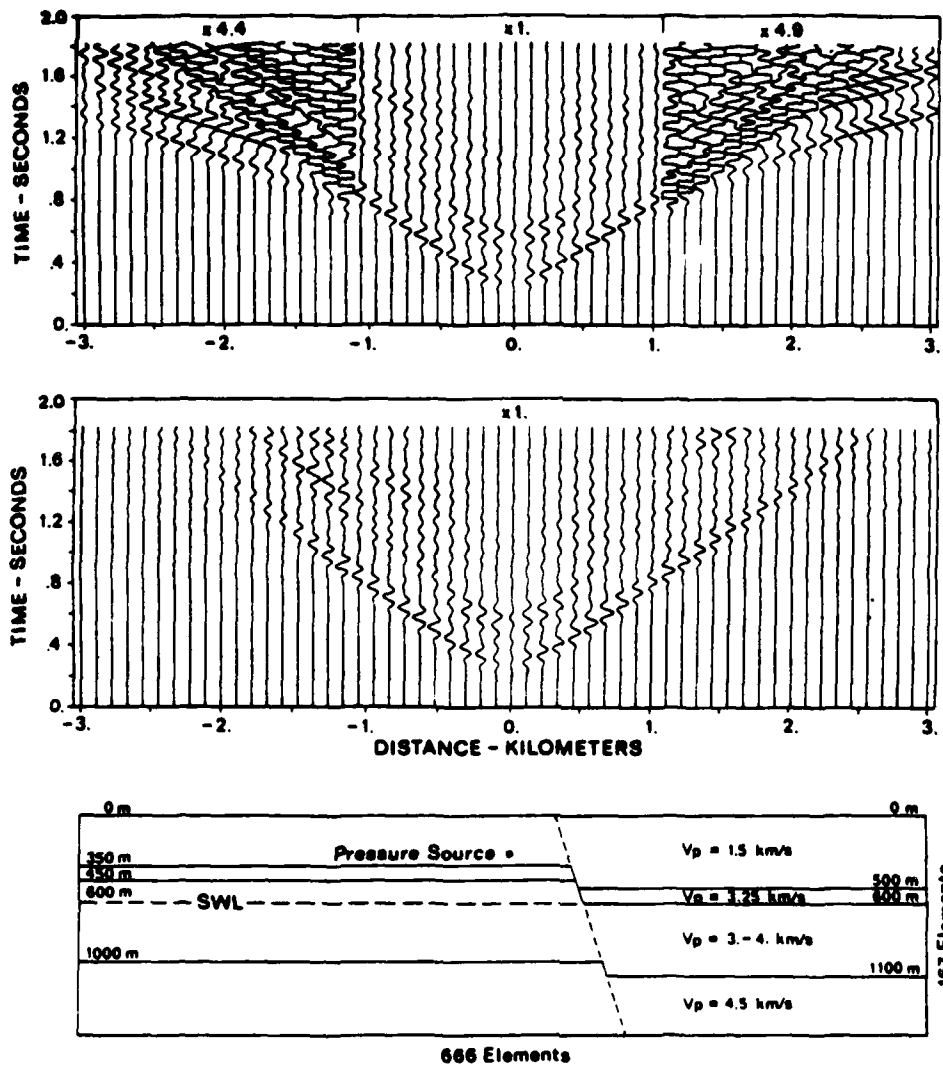


Figure 3.1-2. Horizontal (radial) velocity seismograms over the 2-D COALORA model. Magnifications are indicated above the individual traces.

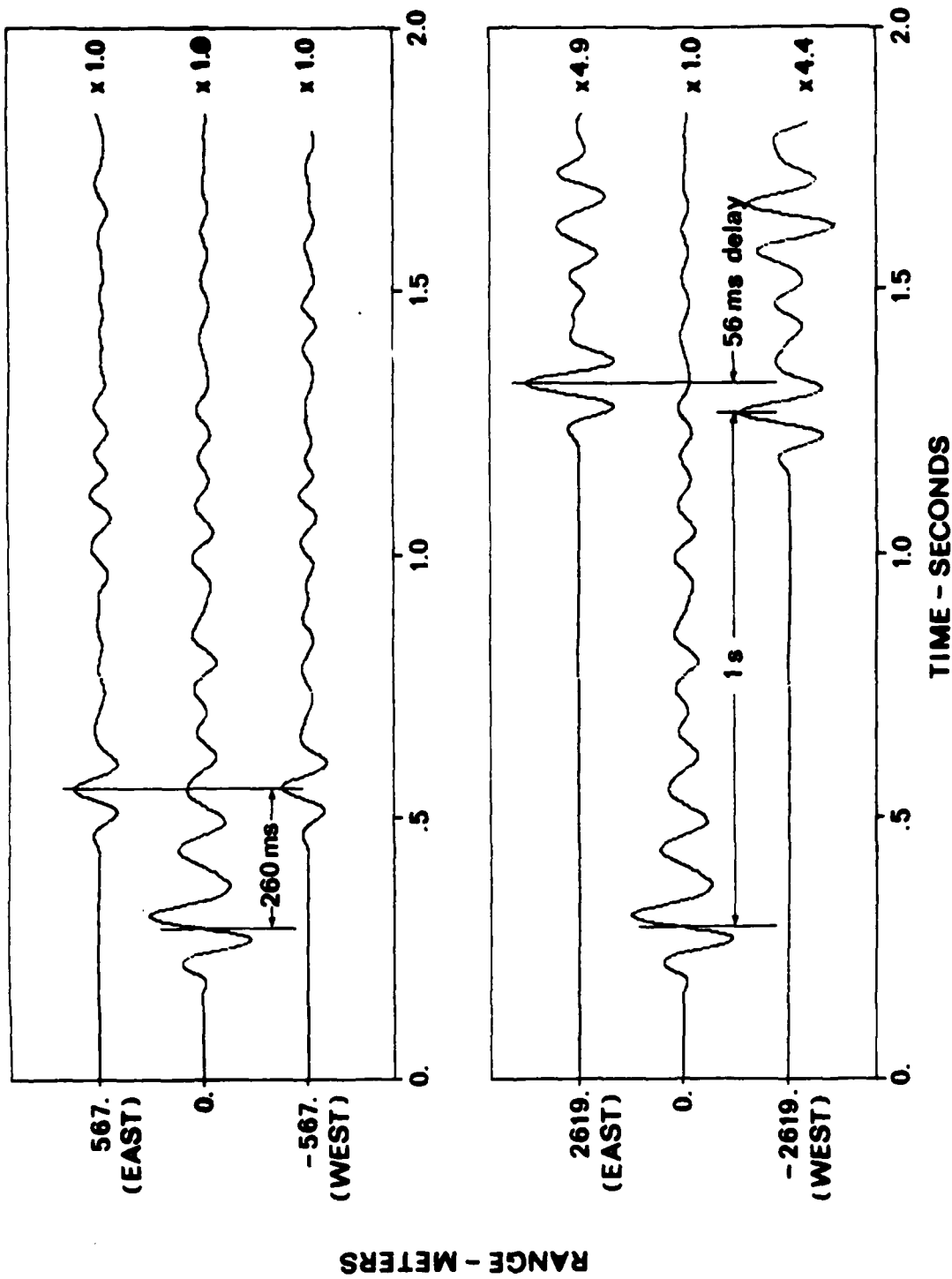


Figure 3.1-3 Vertical velocity seismograms for a 10 Hz wavelet at 600 m and 2619 m ranges east and west of Yucca Fault showing calculated time delays.

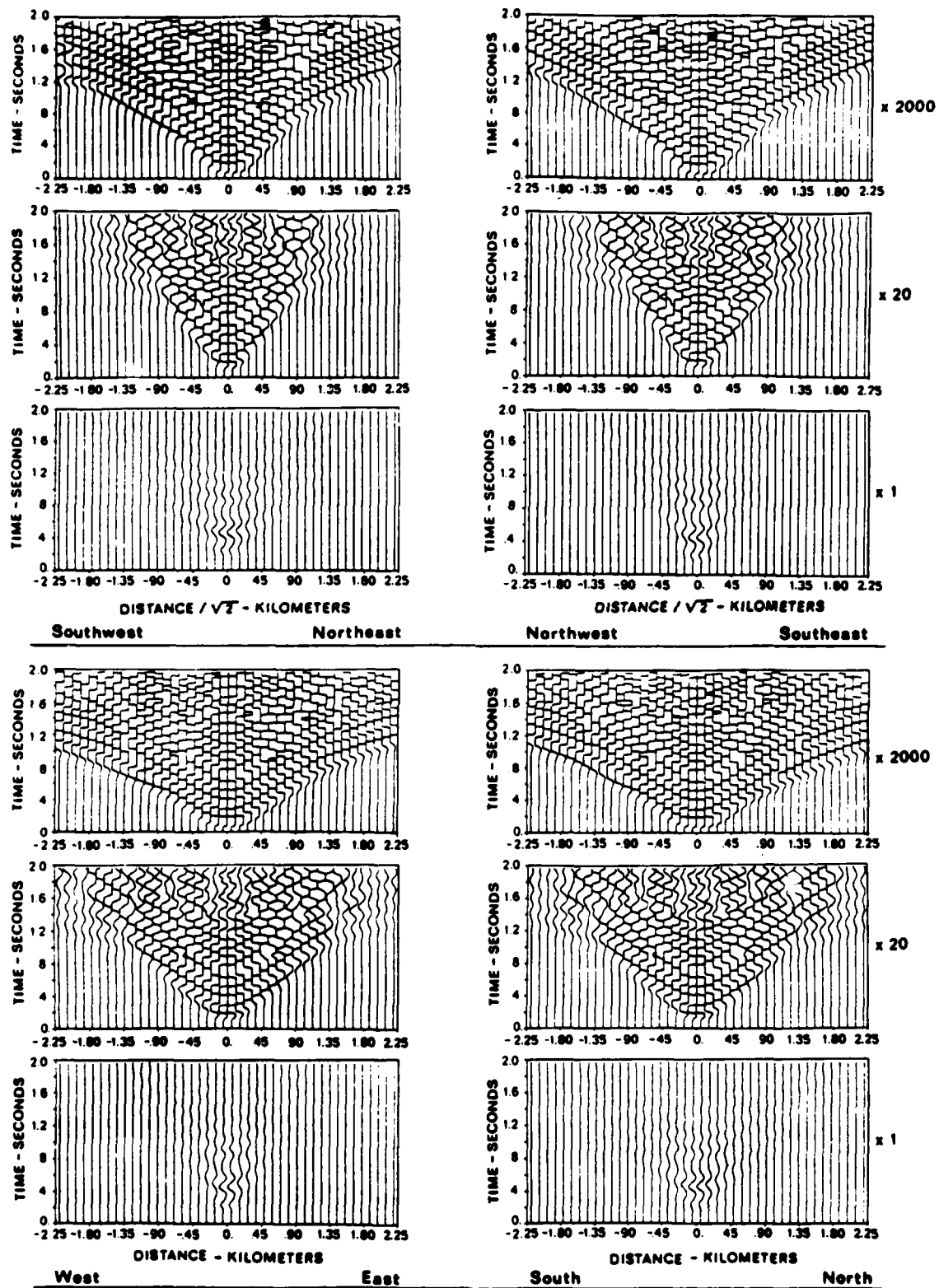


Figure 3.2-1. Vertical velocity synthetic seismograms with magnifications indicated on right. Peak velocity is  $.367 \times 10^{-7}$  m/s and the upper set is for diagonal lines while the lower is for global lines.

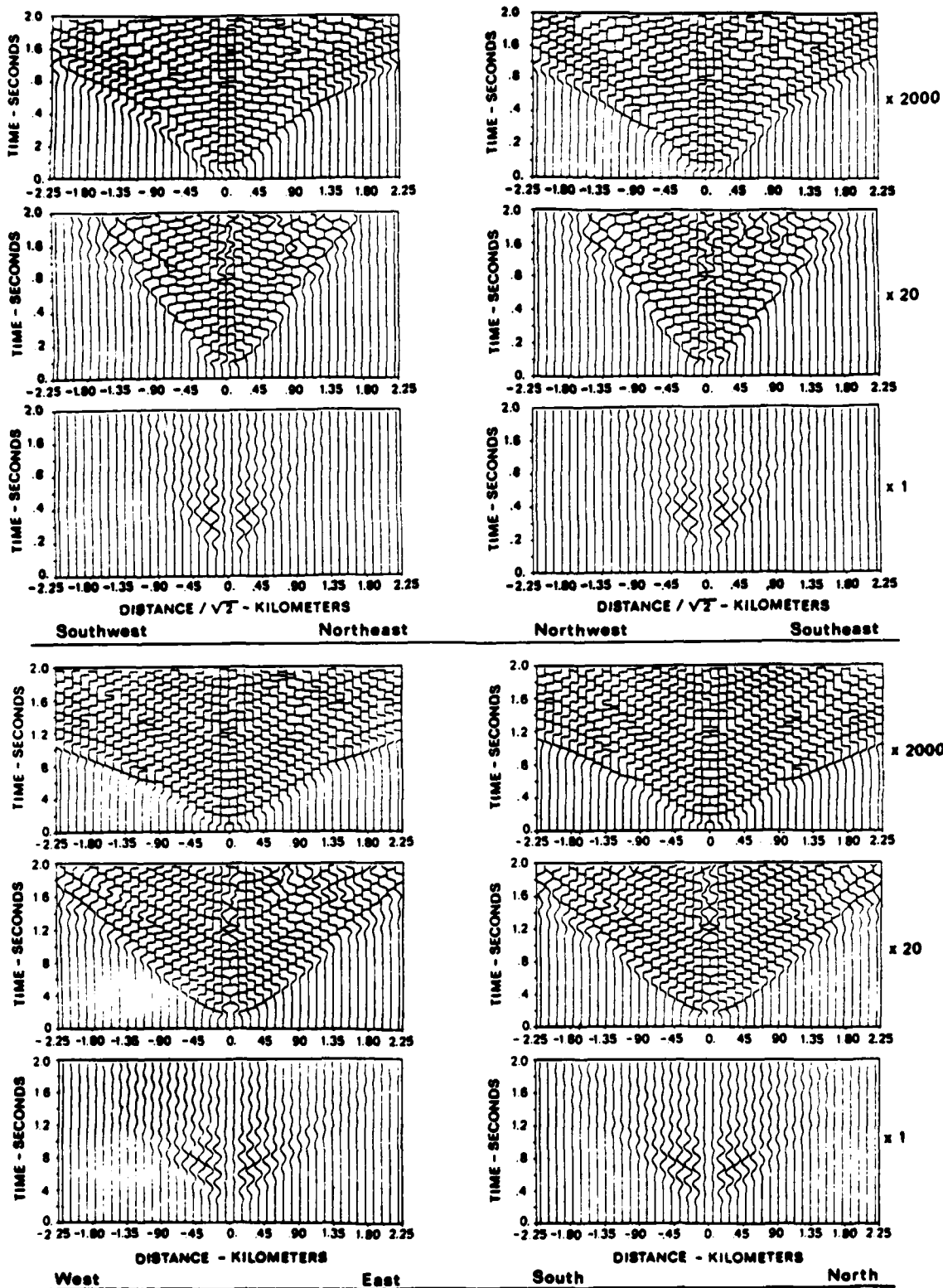


Figure 3.2-2. Radial (horizontal) velocity synthetics. Peak velocity is  $.23 \times 10^{-7}$  m/s.

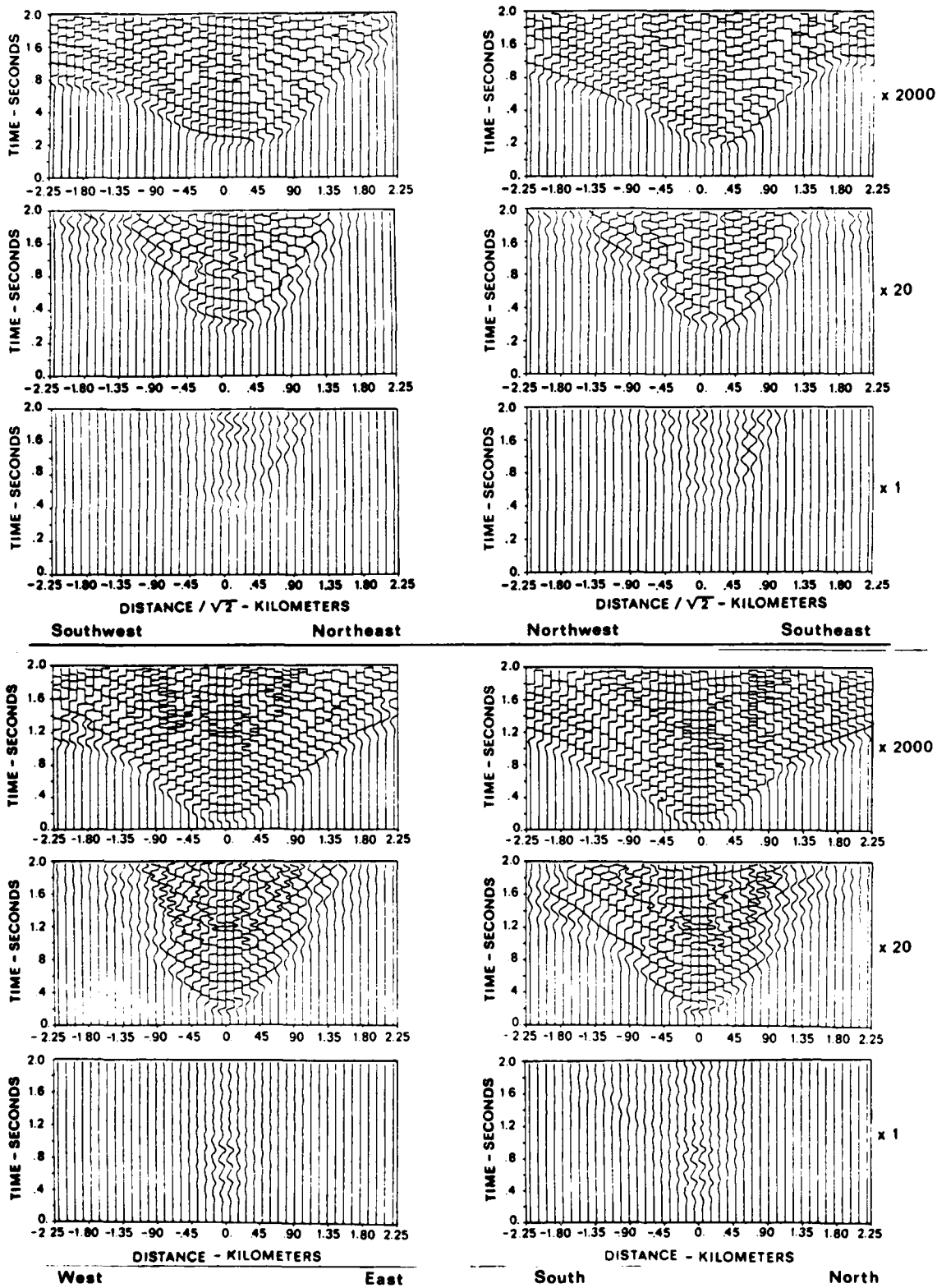


Figure 3.2-3. Transverse velocity synthetics. Peak velocity on global lines is  $.068 \times 10^{-7}$  m/s and on the diagonals it is  $.0107 \times 10^{-7}$  NW-SE and  $.026 \times 10^{-7}$  SW-NE.

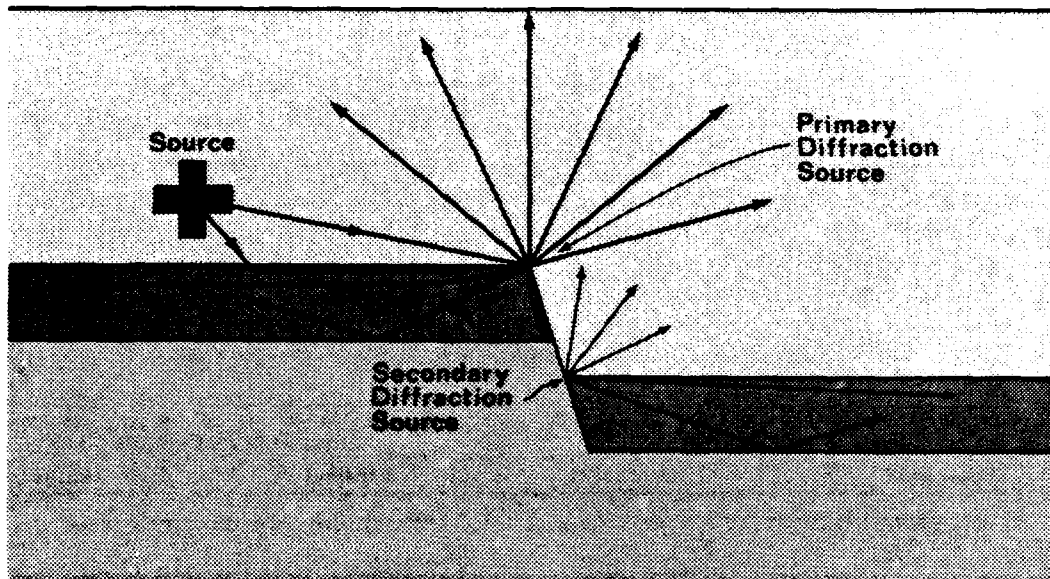


Figure 3.2-4. Drawing of the source and fault discontinuity in the tuff layer showing origin of primary and secondary diffracted waves from the fault edges.

#### 4.0 THEORETICAL ANALYSIS OF THE EXPLICIT WAVE SOLVER

Large-scale simulations of time domain seismic waves in heterogeneous 3-D geology require discrete numerical models with hundreds of thousands to millions of degrees of freedom. Finite difference or finite element methods reduce these models to a large system of ordinary differential equations in time. The simplest explicit integration scheme (lumped mass approximation) provides a natural, as well as practical and efficient algorithm for stepping the system forward in time. The scheme's utility follows from the property that all degrees of freedom are uncoupled during each time-step. This explicit decoupling is a direct expression of the wave-like, i.e., hyperbolic nature of the continuum problem, namely that disturbances at one point take a finite amount of time to influence another point. In the discrete model the decoupling is explicitly implemented by choosing a time-step less than the shortest transit time between any two nodes. The clear advantage over implicit algorithms is that no large coupled system of algebraic equations is necessary. The resulting computer code loops are readily vectorized for optimal processing on pipelined machines.

Explicit integration methods are not without certain disadvantages, however. One is the inherent difficulty in modeling viscous material damping in a manner consistent with the damping behavior of a physical medium. Geologic media are generally characterized by the quality factors,  $Q_\alpha$  and  $Q_\beta$  for dilatational and shear dominated motion, respectively. However, it is not clear using the conventional numerical formulation how to solve for the model damping coefficients as functions of  $Q_\alpha$  and  $Q_\beta$  purely on the basis of nodal field quantities. In other words, given  $Q$ 's over the model, how can viscous damping coefficients for the orthogonal components of nodal velocity be determined? One approach suggested by structural models is to assume so-called Rayleigh damping, e.g., Bathe (1978) where the model damping coefficient is a linear combination of the coefficients multiplying displacement and acceleration vectors, i.e., the stiffness and mass matrices. In its general form of implementation this is a poor approximation for a continuum. However, in terms of a more natural set of local basis vectors (rather than the nodal basis), useful alternatives to Rayleigh damping may be derived.

Another disadvantage to explicit methods is the presence of a class of unrestrained deformational modes, so-called hourglassing modes. These are by-products of the approximate spatial integration scheme used in calculating

nodal field quantities, i.e., internal restoring forces. The modes are associated with linear variations in the field between discrete nodes and can be selectively and artificially restrained after isolating them from the local grid deformations, e.g., Flanagan and Belytschko (1981). Hourglass modes are usually unimportant components of the wave field except near abrupt changes in boundary or loading conditions, or discontinuous 2-D and 3-D geometry like corners and cavities. In the physical model these same discontinuities are strong sources of diffracted waves, implying a correspondence between diffractions and hourglassing. The degree to which hourglass suppression influences calculated diffracted fields is unknown.

In this theoretical section of the report a discrete analyses will be performed to investigate aspects of explicit wave solution theory relevant to the above comments. These include the vector formulation of an explicit finite element algorithm in terms of a very useful modal element basis. This basis extends the theory of hourglass suppression to selective damping of dilatational and shear modes and is derived by diagonalizing the element mass and stiffness matrices.

#### 4.1 THE FINITE ELEMENT EQUATIONS--NODAL BASIS

To optimize the processing of discrete numerical models on pipelined machines, it is necessary to fully vectorize the algorithm while minimizing the number of arithmetic operations. In the following, a straightforward set of vector algebraic equations is derived to accomplish this, based on a somewhat different view of the explicit finite element method. The approach is to reduce the governing element equations to their canonical form by transformations to element deformation basis vectors which diagonalize the mass and stiffness matrices.

The finite element grid used to discretize the model is assumed to be Cartesian, i.e., composed of uniform rectangular elements. Global Cartesian grids provide the simplest formulation possible and eliminate the arithmetic for intermediate element transformations mapping irregular hexahedra to Cartesian boxes. Of course this also eliminates the ability to conform smoothly to irregular (non-Cartesian) boundaries. However, one virtue of large-scale models is that the grid is sufficiently dense to allow good resolution with only stepwise approximations to irregularities. In 2-D this is analogous to the use of many discrete picture elements (pixels) to represent

a graphics image. If the model can resolve a wave pulse of length,  $\lambda$ , then it can also resolve a material inhomogeneity (object) with similar characteristic length. As a consequence, either the highest frequency or smallest object to be represented determines a consistent grid spacing.

The finite element model consists of a three-dimensional, rectangular domain partitioned by a uniform Cartesian grid into identical cubic elements, Fig. 4.1-1. The unknown displacements are to be determined at each grid point or node. Displacements within elements are given by a shape function which interpolates nodal values and maintains continuity between elements.

The simplest shape function for a Cartesian element is a 3-D version of the trapezoidal rule. It can be derived formally from the local 3-D Taylor series expansion by neglecting curvature terms, i.e., terms with second or higher derivatives in one of the space variables. This function gives

$$\begin{aligned} \underline{u}(\underline{x}^c + \underline{\zeta}, t) = & \underline{u}^c + \zeta_1 \underline{u}_{x_1}^c + \zeta_2 \underline{u}_{x_2}^c + \zeta_3 \underline{u}_{x_3}^c + \zeta_1 \zeta_2 \underline{u}_{x_1 x_2}^c \\ & + \zeta_1 \zeta_3 \underline{u}_{x_1 x_3}^c + \zeta_2 \zeta_3 \underline{u}_{x_2 x_3}^c + \zeta_1 \zeta_2 \zeta_3 \underline{u}_{x_1 x_2 x_3}^c \end{aligned} \quad (1)$$

where  $\underline{u} = (u_1, u_2, u_3)^T$  is the displacement vector,  $\underline{x}$  and  $\underline{\zeta}$  are global and local coordinate vectors, respectively, and c superscripts refer to element centroid values. The 24 components of the superscripted vector on the right can be solved in terms of the 24 nodal displacements of the element, giving

$$\underline{u}(\underline{x}^c + \underline{\zeta}, t) = D(\underline{\zeta}) \underline{\delta}(\underline{x}^c, t) \quad (2)$$

where  $\underline{\delta} = (u_{11}, \dots, u_{18}, u_{21}, \dots, u_{28}, u_{31}, \dots, u_{38})^T$  is the nodal displacement vector and subscripts refer to the coordinate and node number, respectively.

With an analytical expression available for displacements within the element, the theory of elasticity gives strains and stress as

$$\begin{aligned} \underline{\epsilon} &= (\epsilon_{11}, \epsilon_{22}, \epsilon_{33}, \epsilon_{12}, \epsilon_{13}, \epsilon_{23})^T \\ &= B \underline{\delta} \end{aligned} \quad (3)$$

$$\begin{aligned} \underline{\sigma} &= (\sigma_{11}, \sigma_{22}, \sigma_{33}, \tau_{12}, \tau_{13}, \tau_{23})^T \\ &= C \underline{\epsilon} = CB \underline{\delta} \end{aligned} \quad (4)$$

where C is the matrix of constitutive constants and B is the strain-displacement matrix, found by differentiating (2) with respect to  $\zeta_1, \zeta_2, \zeta_3$  and substituting into the strain expression,

$$\epsilon_{ij} = \frac{1}{2} \left( \frac{\partial u_i}{\partial \zeta_j} + \frac{\partial u_j}{\partial \zeta_i} \right)$$

The final step applies to principle of virtual work to calculate generalized elastic and inertial forces,  $\underline{f}^E$  and  $\underline{f}^I$  corresponding to the nodal displacements,  $\underline{\delta}$ . For a virtual displacement,  $\underline{\hat{\delta}}$  the elastic work is

$$\int_V \underline{\hat{\epsilon}}^T \underline{\sigma} dv = \int_V \underline{\hat{\delta}}^T \underline{B}^T \underline{C} \underline{B} \underline{\delta} dv$$

and the inertial work due to constant mass density,  $\rho$  is

$$\int_V \underline{\hat{u}}^T (\rho \underline{\ddot{u}}) dv = \int_V \underline{\hat{\delta}}^T \underline{D}^T \rho \underline{D} \underline{\ddot{\delta}} dv$$

External work of the elastic and inertial nodal forces are  $\underline{\hat{\delta}}^T \underline{f}^E$  and  $-\underline{\hat{\delta}}^T \underline{f}^I$ , respectively. Equating these to the integrals and solving gives

$$\underline{f}^E = \underline{K} \underline{\delta}, \quad \underline{K} \equiv \int_V \underline{B}^T \underline{C} \underline{B} dv \quad (5)$$

$$\underline{f}^I = -\underline{M} \underline{\ddot{\delta}}, \quad \underline{M} \equiv \rho \int_V \underline{D}^T \underline{D} dv \quad (6)$$

where K and M are the symmetric stiffness and mass matrices and the integrals are over element volume. Therefore, the discrete system of equations governing motion of the single finite element is, from dynamic equilibrium,  $\underline{f}^E = \underline{f}^I + \underline{g}$ , hence

$$\underline{M} \underline{\ddot{\delta}} = -\underline{K} \underline{\delta} + \underline{g} \quad (7)$$

where  $\underline{g}$  represents the influence of adjacent elements, external forces and damping. The 24 x 24 matrices are easily evaluated and K is found to be fully populated while M consists of three 8 x 8 blocks on the main diagonal.

#### 4.2 THE FINITE ELEMENT EQUATIONS--MODAL BASIS

Element stiffness and inertia properties can be defined with respect to any complete set of displacement modes. The nodal basis used above is ideal for deriving the system but not necessarily for optimal computational efficiency. For the latter purpose, it is necessary to carefully examine the structure and symmetries of the system of 24 equations governing a single

element. A formal diagonalization of the mass and stiffness matrices would yield the forms,

$$M = PMP^T \quad (8)$$

$$K = QXQ^T \quad (9)$$

where P and Q are matrices of eigenvectors and  $\mathcal{M}$  and  $\mathcal{K}$  are diagonal eigenvalue matrices. This is an effective approach but the required eigenvalue-eigenvector analysis is non-trivial. Fortunately, a simpler alternative exists.

The alternative is to diagonalize the matrices by inspection, on the basis of displacement modes of a unit cube. It is natural to start with the mass matrix, M, because of its block structure. The three 8 x 8 blocks are each associated with one component of nodal displacement so only one block need be considered, the others following by a permutation of indices. To proceed, recall that formal diagonalization of square matrices and modal analysis of discrete structures share the same underlying mathematics, differing only in viewpoint. Therefore, diagonalization of the block matrices may be achieved by a single modal analysis of the cube under the constraint that only one component of displacement is involved. These modes consist of a rigid body translation and seven deformations. The modal shapes are represented by their eight ordered nodal displacements in vector form and all modes are orthogonal (i.e., scalar products vanish).

The seven deformation modes are of two kinds. The first kind includes the three modes familiar from classical elasticity theory--one extension (or compression) and two shears in say, the  $\zeta_1$ , direction. The second kind consists of four so-called hourglass modes. These are less familiar because they represent bending deformations which are higher order and therefore vanish in the usual mathematical limiting process with respect to modes of the first kind. Modes of the second kind are encountered in the couple-stress theory of elasticity, Sternberg (1968) which provides a natural theoretical basis for their further study.

The complete set of mass matrix modes for the cube is plotted in Fig. 4.2-1, where each is represented by its proportional modal displacement vector,  $S_n^i$ ,  $n = 1-8$  and  $i = 1$  for the  $\zeta_1$ , direction. The rigid body mode is a vector with all elements equal. Modes of the first kind are given by vectors with elements proportional to the  $\zeta_1$ ,  $\zeta_2$ , and  $\zeta_3$  nodal coordinates,

respectively, in the cube-centered Cartesian coordinate system, Fig. 4.1-1. Modes of the second kind may be derived by an orthogonalization process starting from the four known orthogonal mode vectors (1 rigid body and 3 first kind), e.g., Gram-Schmidt orthogonalization, or by simple experimentation. They are also available in the literature, e.g., Flanagan and Belytschko (1981).

To diagonalize the mass matrix the block modal or eigenvector matrix is formed as  $P_i = (S_1^i \dots S_8^i)$  from which the similarity transformation, P in (8) becomes

$$P = \frac{1}{2^3} \begin{pmatrix} P_1 & 0 & P \\ 0 & P_2 & P \\ 0 & 0 & P_3 \end{pmatrix} \quad (10)$$

The  $P_i/2^3$  and P matrices are unitary (orthogonal) meaning that  $P^{-1} = P^T$ . The diagonalized mass matrix can therefore be written as

$$\mathcal{M} = P^T M P$$

Diagonalization of the stiffness matrix proceeds by first applying the similarity transformation for the mass matrix, P as

$$\bar{K} = P^T K P$$

Detailed analysis and results from the interim report, Wojcik, et al. (1982) show that  $\bar{K}$  is considerably simpler than K, but not yet diagonal. The number of nonzero elements is reduced from 576 in K to 39 in  $\bar{K}$  because of the greatly simplified stress state for the element modes in Fig. 4.2-1. The 18 off-diagonal terms arise from coupling of the  $\zeta_1$ ,  $\zeta_2$  and  $\zeta_3$  components of the modes of the first kind, i.e., coupling between the three extensional modes and between the six shear modes. Modes of the second kind are uncoupled. Therefore it is necessary to diagonalize the reduced system as

$$\mathcal{K} = R^T \bar{K} R$$

where matrix R is determined by generalizing the 2-D results obtained in the interim report. In particular, the 9 modes of the first kind (3 modes in 3 directions) can be decomposed into 3 Poisson stretch modes, 3 pure shear modes and 3 rigid rotation modes. These stiffness modes are drawn in Fig. 4.2-2 for the  $\zeta_1$  direction and can be written in terms of linear combinations of mass modes of the first kind, resulting in an expression for R

consisting of constants in the nonzero locations of  $\bar{K}$ . Therefore, the diagonal stiffness matrix becomes

$$\kappa = R^T P^T K P R = Q^T K Q$$

In terms of the above factorization of the mass and stiffness matrices, the equations for a simple finite element become

$$P M P^T \ddot{\delta} = -P R \kappa R^T P^T \delta + g \quad (11)$$

Therefore, to solve for the nodal accelerations, it is only necessary to pre-multiply through by the inverse of the factored mass matrix, i.e.,  $P M^{-1} P^T$ , giving

$$\ddot{\delta} = P M^{-1} R \kappa R^T P^T \delta + P M^{-1} P^T g \quad (12)$$

This is a new form of the consistent mass equation for nodal acceleration--new in terms of the simple factorization of  $M^{-1} K$  multiplying  $\delta$ . In most practical applications to continua, the consistent mass matrix,  $M$  is replaced by a diagonal lumped mass approximation,  $\hat{M}$  to allow a trivial inversion of  $\hat{M}$ , hence a solution for  $\delta$ . This yields

$$\ddot{\delta} = \hat{M}^{-1} P R \kappa R^T P^T \delta + \hat{M}^{-1} g \quad (13)$$

neglecting the external force vector,  $g$  and comparing the consistent mass equation, (12) to the lumped mass approximation, (13) shows that in terms of arithmetic operations there is no advantage to mass lumping in the above formulation.

#### 4.3 VISCOUS DAMPING

There remains the question of a consistent viscous damping term in the finite element equations of motion. To make the damping term explicit in our formulation the force vector,  $g$  is replaced by

$$g \rightarrow -C \dot{\delta} + g$$

The unknown damping matrix,  $C$  is factored as

$$C = S C S^T$$

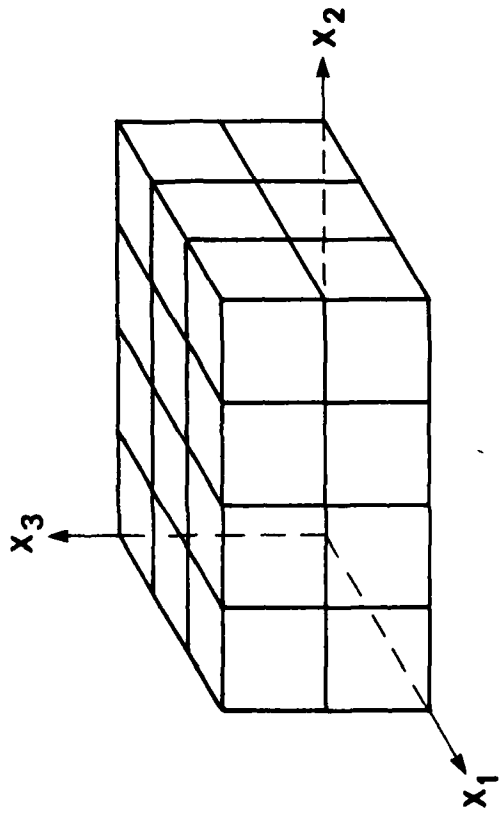
where  $C$  and  $S$  are its eigenvalue and eigenvector matrices. The intent is to damp extensional and shearing motions of the medium, so it is natural to consider the case where  $S = Q$ , i.e., where the damping matrix has the same eigenvectors as the stiffness matrix. The eigenvalues of  $C$  therefore consist

of the damping coefficients of the individual modes in the stiffness bases-- the rigid translations and rotations, Poisson extensions, pure shears and the stress-couple or hourglass modes. It follows that each of these modes of a finite element can be selectively damped by choosing an appropriate constant for each eigenvalue of C in the stiffness basis.

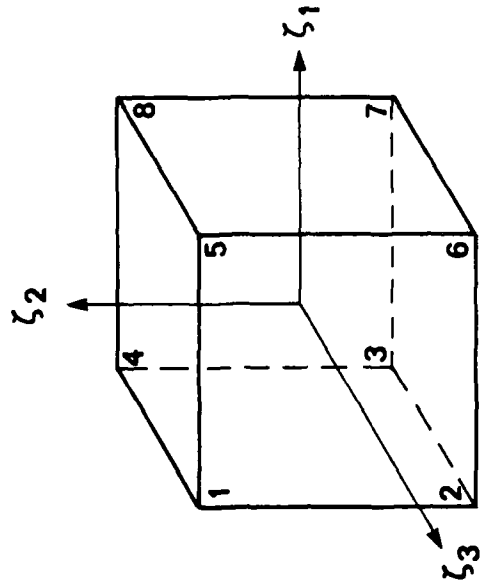
The resulting damped finite element equations become, from (11),

$$PMP^T \ddot{\delta} + QCQ^T \dot{\delta} + QXQ^T \delta = g \quad (14)$$

In practice the only modes for which damping data is available are the extensional and shear modes. In order to evaluate the damping constants in (14) from the given quality factors,  $Q_\alpha$  and  $Q_\beta$  (or alternatively, given percentages of critical damping), exact solutions for the natural frequencies of the Poisson extension and pure shear modes are necessary. These can be obtained from a vibrational analysis of the two deformation modes in Fig. 4.2-2.



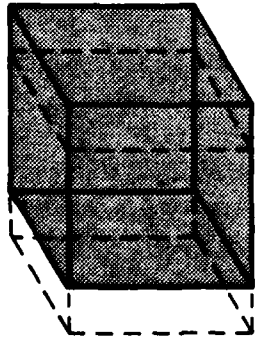
**Cartesian Grid**



**Element Coordinate System**

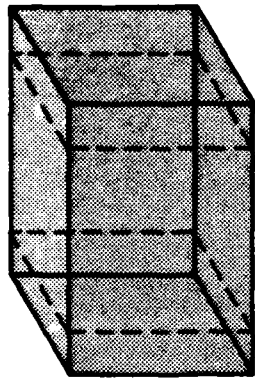
Figure 4.1-1. The Cartesian grid and element coordinate system assumed for isotropic media.

TRANSLATION



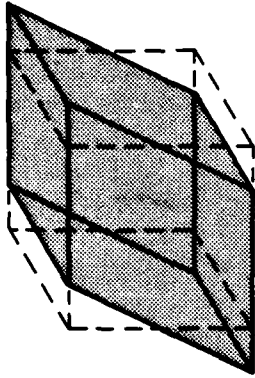
$$S_1^1 = (1, 1, 1, 1, 1, 1, 1, 1)^T$$

EXTENSION

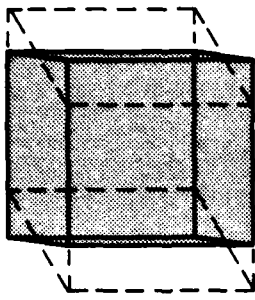


$$S_2^1 = (-1, -1, -1, -1, 1, 1, 1, 1)^T$$

SHEAR

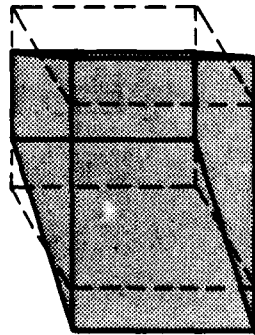


$$S_3^1 = (1, -1, -1, 1, 1, 1, -1, -1)^T$$

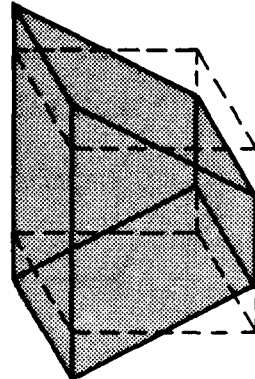


$$S_4^1 = (1, 1, -1, -1, 1, 1, -1, -1)^T$$

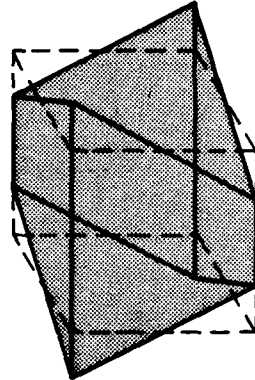
BENDING



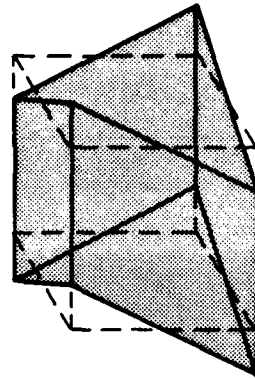
$$S_5^1 = (1, -1, 1, -1, 1, -1, 1, -1)^T$$



$$S_6^1 = (-1, -1, 1, 1, 1, 1, -1, -1)^T$$



$$S_7^1 = (-1, 1, 1, -1, -1, -1, 1, 1)^T$$



$$S_8^1 = (-1, 1, -1, 1, 1, -1, 1, -1)^T$$

Figure 4.2-1. The eight mass matrix deformation modes of a cube, for the  $\zeta_1$  direction. Extension and shear are modes of the first kind, while bending deformations are modes of the second kind.

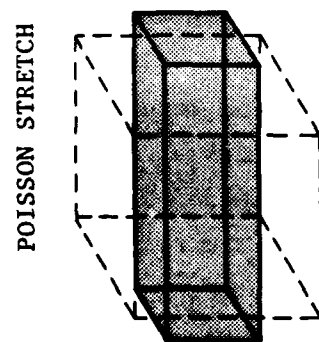
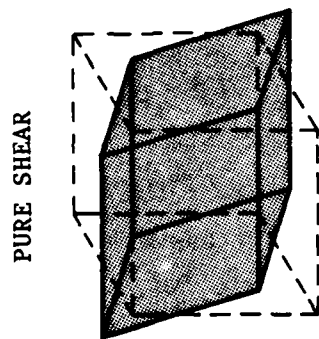
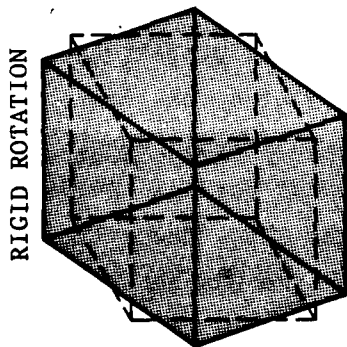


Figure 4.2-2. The decomposition of extension and shear modes into Poisson stretch, pure shear and rotation modes, shown here for the  $\zeta_1$  direction.

## 5.0 CONCLUSIONS

The conclusions drawn from this research effort concern: large-scale numerical modeling of seismic waves on supercomputers; a geophysical data base adequate to justify 3-D simulations and interpretations of very near-field seismic events; and a theoretical study of specializations of the explicit finite element algorithm used for the calculations. The primary conclusion is that, given the three-dimensional geologic database available from past and ongoing investigations in Yucca Flat, Nevada Test Site, the size of feasible 3-D computational models on the CRAY-1S appears to be adequate to simulate full elastic wave fields and interpret arrivals for comparison with existing 3-D ground motion data. The most significant shortcoming is lack of an analytical implementation of the 3-D pressure source. Instead, a relatively crude discretization of the source cavity is pressurized, producing some artificial asymmetry in the outgoing pressure pulse. Thus the discrete source in 3-D requires further investigation and characterization. In two dimensions, much higher grid density is available for modeling so that discretization errors are not significant in large-scale 2-D applications.

Synthetic seismograms from the 3-D simulation of the COALORA event at Yucca Flat indicate that a significant source of transverse motion on radial lines through the source is diffraction from abrupt changes in geology. In our model, diffractions were observed from the discontinuity in the Rainier Mesa layer across the Yucca fault. This suggests that local geologic inhomogeneities near the source will act as simple diffraction sources--effectively providing secondary seismic sources in the free-field. This is in contrast to the mechanisms of free-field scattering and strain release which can also contribute to transverse motion. Future large-scale calculations of plane waves through a detailed 3-D inhomogeneous model in Yucca Flat would enable us to quantify the strength of the diffracted transverse motion.

Regarding diffracted fields, their representation by explicit finite element methods requires further investigation. The reason is that the pressurized source and material discontinuities produce hourglass modes which are artificially suppressed during computations. However, we observe that diffraction and hourglassing are closely associated because they are produced

by similar features, namely discontinuities in loading or geometry. Therefore, what is the effect of hourglass suppression on real diffracted waves? The answer to this question must come from a theoretical study of the finite element algorithm.

Successful time-domain simulations in 3-D are clearly feasible with pipelined supercomputers. Optimal processing still requires careful tailoring of the algorithm, however, to vectorize inner code loops and eliminate nonessential arithmetic. An effective approach to simplify the implementation and theory is to use dense Cartesian grids, typical of finite difference methods, to discretize the model. The simplest case is the uniform grid consisting of cubic elements--used exclusively in the present study. Theoretical analysis of the cubic finite element shows that the application of heuristic eigenvalue-eigenvector concepts, i.e., a change of basis, yields a closed form diagonalization of the element mass and stiffness matrices. This provides a drastic reduction in the number of floating point operations required to evolve the element forward in time.

In addition to the arithmetic simplifications provided by the eigenvalue-eigenvector element modal analysis, the resulting displacement basis admits selective damping of the individual vibrational modes of the element. Consistent viscous damping has always been a problem with explicit finite elements, but the modal basis on cubic elements appears to yield an effective approach, worthy of further investigation. The modal basis also allows a consistent mass formulation with the same number of arithmetic operations as the lumped mass approximation, as well as an exact integration to produce the stiffness matrix. For comparison, the FLEX code used for the present calculations (representative of state-of-the-art explicit finite element theory) is formulated with lumped masses and approximate single point Gaussian integration. All of these theoretical simplifications derive from the cubic element and the application of linear algebra techniques to the element matrices.

Regarding hourglass suppression and its influence on diffractions, an examination of the element modes shows 12 so-called hourglass modes for a cube. These modes are involved with bending of the element due to moments or couples acting on the element faces. However, the hourglass modes of a cube are not complete, hence overly stiff, because curvature terms are excluded from the element shape function. By including 12 curvature terms in the

Taylor series (2 for each face) and 12 additional generalized displacements, a consistent bending theory can be derived. The appropriate generalized displacements are expected to be the 12 edge rotations. Rotations are usually included in plate bending theories using Hermite polynomials, but a similar inclusion in 3-D continuum theories appears to be new. We observe that bending modes are associated with the couple-stress formulation in elasticity theory, e.g., Mindlin (1963), Sternberg (1968). Couple-stress theory has been thoroughly studied but is of limited utility; however, the present work indicates that it may provide a further analytical framework for assessing the effect of hourglass control on diffractions.

## REFERENCES

1. Bathe, K.-J. and E. L. Wilson (1976). Numerical Methods in Finite Element Analysis, Prentice-Hall, Inc.
2. Battis, J. (1981). Seismic Velocity Models for Western Alluvial Basins, Environmental Research Papers, No. 740, Terrestrial Sciences Division, Air Force Geophysics Laboratory.
3. Cogbill, A. and F. App (1983). Personal Communication, Containment Group, LANL.
4. Ferguson, J. F. (1983). Personal Communication, University of Texas, Dallas.
5. Ferguson, J. F. and E. Herrin (1982). Variations in Body Wave Magnitude For Yucca Flat, Nevada Explosions, in the Final Tech. Report for AFOSR Contract F49620-81-C-0010 Geophysics Laboratory, Southern Methodist Univ.
6. Fernald, A. T., et al. (1967). Surficial Deposits of Yucca Flat Area, Nevada Test Site, in Nevada Test Site, Memoir 110, The Geological Society of America, Inc.
7. Flanagan, D. P. and T. Belytschko (1981). A Uniform Strain Hexahedron and Quadralateral with Orthogonal Hourglass Control, Int. Journal for Numerical Methods in Engineering, 17.
8. Haskell, N. A. (1967). Analytical Approximation for the Elastic Radiation from a Contained Underground Explosion, J. Geophys. Res., 72.
9. Love, A.E.H. (1944). A Treatise on the Mathematical Theory of Elasticity, Dover Publications, New York.
10. Mindlin, R. D. (1963). Influence of Couple-Stresses on Stress Concentrations, Experimental Mechanics, 3(1).
11. Sternberg, E. (1968). Couple-Stresses and Singular Stress Concentrations in Elastic Solids, Proceedings of IUTAM Symposium on the Generalized Cosserat Continuum, Springer-Verlag, New York,
12. Stump, B. (1983). Personal Communication, Southern Methodist University.
13. Stump, B. and R. E. Reinke (1983). The COALORA Near Field Experiment, AFWL NETESC, Kirtland AFB,. Presented at Fifth annual DARPA/AFOSR Seismic Research Symposium, May 1983.
14. Wojcik, G. L., J. Isenberg, D. K. Vaughan and R. E. Wolf (1982). Large-Scale Numerical Analysis of Seismic Waves in Basins, Interim Report AFOSR Contract F49620-82-C-0002 Weidlinger Associates.

END

RECEIVED